Supplementary Materials for

J_{eff} = ½ Diamond Magnet $CaCo_2TeO_6$: Reimagining Frontiers of Spin Liquids and Quantum Functions

Xudong Huai,[1] Luke Pritchard Cairns,[2] Bridget Delles,[1] Michał J. Winiarski,[3] Maurice Sorolla II,[4] Xinshu Zhang,[5] Youzhe Chen,[2] Stuart Calder,[6] Eun Sang Choi,[7] Tatenda Kanyowa,[8] Anshul Kogar, [5] Huibo Cao,[6,8] Danielle Yahne,[6] Robert Birgeneau,[2] James Analytis,[2] Thao T. Tran*[1]

*thao@clemson.edu

The PDF file includes:

Experimental Section

Reagents

The starting materials are $CaCO_3$ (Acros organics, 99%), $CoCO_3$ (Alfa Aesar, 99.5%), $Te(OH)_6$ (Tokyo Chemical Industry, 99.0%), and TeO_2 (Alfa Aesar, 99%).

Synthesis

A small amount of crystal is first prepared by flux growth. $CaCO_3$, $CoCO_3$, and $Te(OH)_6$ powder (molar ratio 2:2:5) was ground and pressed into a pellet. The pellet is then sent to a box furnace, heated at 850°C, followed by slow cooling. With the crystal, we acquired the melting point (625°C) and decomposition point (800°C) of $CaCo_2TeO_6$ by conducting TGA-DSC measurements.

With the melting point confirmed, the polycrystalline sample was prepared by a solid-state reaction. A stoichiometric mixture of $CaCO_3$, $CoCO_3$, and $Te(OH)_6$ powder was ground and pressed into a pellet and then placed in a box furnace with the temperature set at 625 °C for eight days with multiple grinding and pelletizing. Powder XRD is then performed on this pinkish-purple powder, and the structure of the polycrystalline sample is confirmed by Rietveld refinement.

High-quality crystal samples were then synthesized by flux growth method by heating polycrystalline $CaCo_2TeO_6$ and TeO_2 as flux (molar ratio 2:5) at 900°C for 40 h followed by slow cooling. Block-shaped dark blue crystals can be separated from the transparent flux. The reason why $Te(OH)_6$ is not selected as self-flux is because its molten phase does not have enough mobility to dissolve $CaCo_2TeO_6$.

Single-Crystal X-ray Diffraction

Single-crystal XRD experiments were performed on $CaCo_2TeO_6$ using a Bruker D8 Venture diffractometer with Mo Kα radiation ($\lambda = 0.71073$ Å) and a Photon 100 detector at $T = 300$ K. Data processing (SAINT) and scaling (SADABS) were performed using the APEX3 software. The structure was solved by the intrinsic phasing 2 method (SHELXT) and refined by full-matrix least-squares techniques on F2 (SHELXL) using the SHELXTL software suite. All atoms were refined anisotropically.

Synchrotron X-ray Diffraction

A synchrotron XRD pattern of $CaCo_2TeO_6$ was collected using the 11-BM beamline at Advanced Photon Source, Argonne National Laboratory. Data were collected using a well-grounded crystal of $CaCo_2TeO_6$ at $T = 295$ K and $\lambda = 0.45789$ Å. Rietveld refinement of the XRD pattern was performed using TOPAS Academic V6. [1, 2] Vesta software was used for crystal structure visualization.

Vis-NIR Spectroscopy

$CaCo_2TeO_6$ powder is ground with PTFE and pressed into a pellet. The reflectance is then measured from 2500 – 480 nm (0.5 – 2.5 eV) by Agilent Cary 7000 UV-Vis-NIR spectrometer.

Second Harmonic Generation (SHG)

We performed second harmonic generation spectroscopy on $CaCo_2TeO_6$ in transmission configuration. The incident light pulse was generated by an optical parametric amplifier with tunable wavelength 950-1030 nm (roughly 1.2-1.3eV). The incident light was focused normally on the sample with a 100 μm spot size, and the fluence was kept below 1 mJ/cm^2 to minimize heating. The light interacting with the sample generated a second harmonic radiation. The detection of the second harmonic light was conducted with a commercial photo-multiplier tube. The sample temperature can be varied from 4 K to 300K with a standard optical cryostat.

Magnetization and Specific Heat

DC magnetization measurements on $CaCo_2TeO_6$ powder were performed with the vibrating sample magnetometer (VSM) option of Quantum Design Physical Properties Measurement System (PPMS). AC magnetization was measured using the ACMS option. Magnetic susceptibility was approximated as magnetization divided by the applied magnetic field: $\chi \approx M/H$. Specific heat measurements were performed using a Quantum Design PPMS Dynacool with ^{3}He insert for $T > 1$ K and a home-built dilution refrigerator setup for $T < 1$ K. The data was acquired using the relaxation time method across the full temperature range.

High-field Magnetization

Orientation-dependent high-field magnetization measurements of $CaCo_2TeO_6$ were performed on a 13.73 mg single crystal using a conventional VSM coupled with a water-cooled resistive magnet in Cell 8 of the DC Field Facility at the National High Magnetic Field Laboratory (NHMFL) in Tallahassee, Florida. The VSM was calibrated against a nickel-standard sphere, and the sample was mounted on a brass holder using 3.5 mm quartz rods and GE-7031 varnish. To further calibrate the temperature and field, the resulting magnetization data were normalized by comparing them with a DC magnetization curve obtained via a VSM in a 16 T PPMS (Quantum Design) at NHMFL.

Powder Neutron Diffraction

A 5 g powder sample of $CaCo_2TeO_6$ was pressed into pellets and loaded into an Al can, then backfilled with 1 atm He. The sample was then loaded into a cryomagnet on the HB-2A powder diffractometer at ORNL. Measurements were performed down to 1.6 K and up to 6 T magnetic field with the 2.41 Angstrom (Ge113) incident wavelength in the open-open-21' collimator setting. Magnetic structure determination was done using the FullProf[3] software suite, utilizing the Bilbao Crystallographic Server for the magnetic space group formalism, and SARAh Representational Analysis software for the irreducible representation formalism.

Single-crystal Neutron Diffraction

Single-crystal neutron diffraction measurements were conducted at CORELLI at the Spallation Neutron Source (SNS) at Oak Ridge National Laboratory. A single crystal (~3 mg) was mounted in a Closed-Cycle Refrigerator (CCR) for low-temperature measurements. Diffraction data were collected by rotating the crystal around the instrument's vertical axis. Measurements were taken during cooling ($T > 17$ K) and at $T = 15$ K. The difference between these datasets can be used to identify the ordered magnetic phase at 15 K. The well-indexed reciprocal space directly reveals the propagation vector of the magnetic order, which is difficult to determine from powder diffraction data. Structural refinement was performed using the FullProf Suite [3].

Density Functional Theory Calculation

Spin-polarized electronic structure calculations for $CaCo_2TeO_6$ were performed using a full-potential linearized augmented plane wave (FP-LAPW) method as implemented in the WIEN2k code[4]. The exchange-correlation potentials were treated within the density functional theory (DFT) using the Perdew−Burke−Ernzerhof generalized gradient approximation (PBE-GGA).[5] The self-consistencies were performed using 720 k-points (10 × 9 × 8 mesh) in the irreducible Brillouin zone. To correct for electron over-delocalization, a 9 eV, Hubbard U correction was applied for Co-*d* bands. The muffin-tin radius values 1.13, 1.22, 0.97, and 0.83 Å were used for Ca, Co, Te and O, respectively.

Pseudopotential band structure and polarized density of sates were calculated for $CaCo_2TeO_6$ and $CoRh_2O_4$ using the pw.x program in the Quantum Espresso (QE) software package,[6] with the Generalized Gradient Approximation of the exchange-correlation potential and Hubbard U correction (GGA+U) for Co-*d* orbital (9 eV) of the exchange-correlation potential with the PBEsol parametrization. Projector-augmented wave (PAW) potentials for Rh, Ca, Co, Te and O were taken from the PSlibrary v.1.0.0 set[7]. The applied k-mesh for $CaCo_2TeO_6$ is the same as in WIEN2k calculations, and a 8 × 8 × 8 mesh was used for $CoRh_2O_4$. The kinetic energy cutoff for charge density and wavefunctions was set to 40 eV and 450 eV for $CaCo_2TeO_6$ (47 eV and 480 eV for $CoRh_2O_4$, respectively). The PAW wavefunctions calculated from the QE package are projected into a linear combination of atomic orbitals (LCAO) based representation by means of the Local Orbital Basis Suite Towards Electronic-Structure Reconstruction (LOBSTER) program[8, 9] to extract the projected crystal orbital Hamilton populations (-pCOHP). [10, 11]

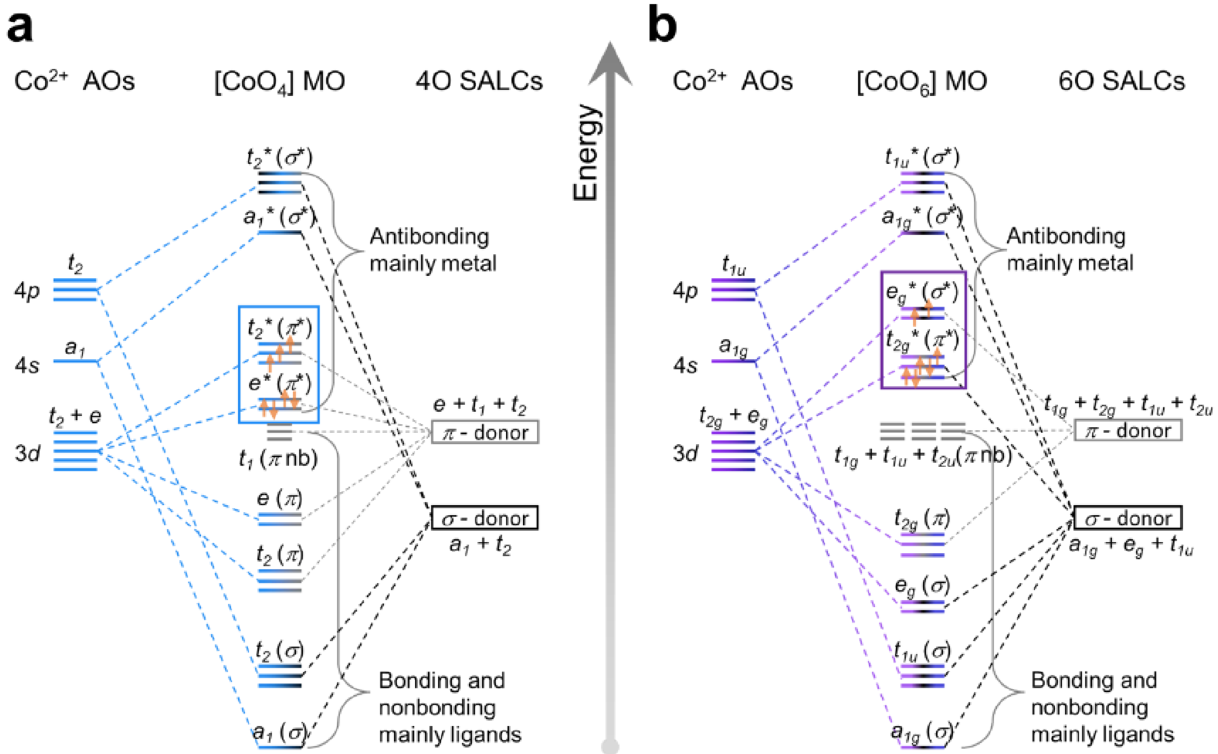

Figure S1. Molecular orbital interaction diagram for (a) T_d-[CoO_4] and (b) O_h-[CoO_6].

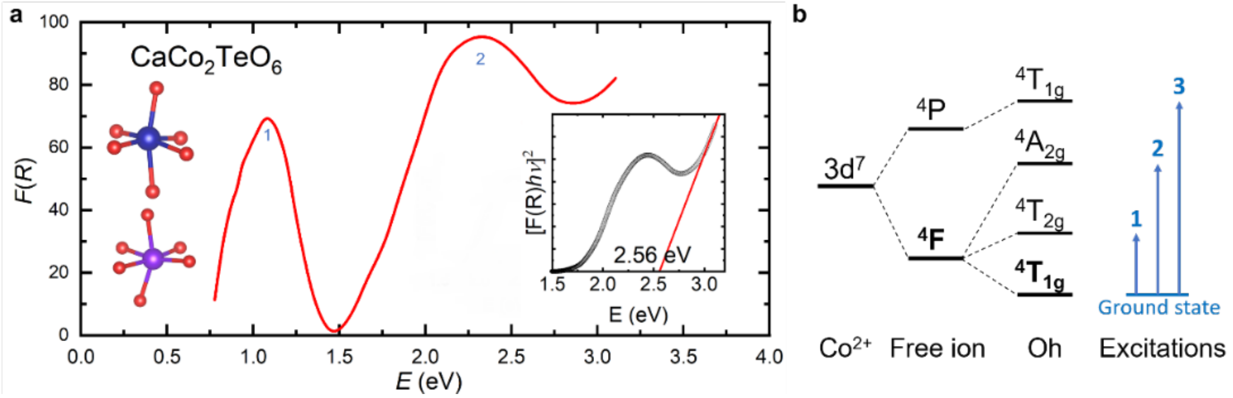

Figure S2. UV-Vis-NIR spectroscopy and the optical gap.

The obtained spectral profile (a) shows that the environments of Co^{2+} ions closely resemble a near-ideal octahedral geometry (b). The optically determined band gap correlates well with the observed blue color of the crystal. Further insight is provided by the crystal field splitting diagram presented in Figure 1d, which elucidates the corresponding absorption (F(R)) spectrum observed.

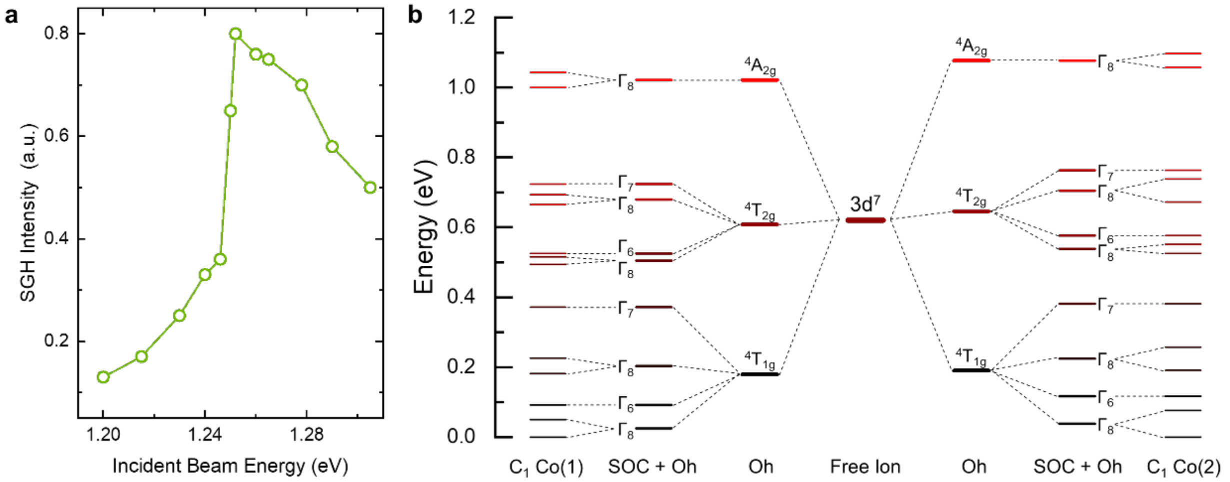

Figure S3. SHG spectrum and calculated crystal orbital splitting diagram with spin orbital coupling.

As the incident light resonates with the crystalline effect field (CEF) level of the materials (calculated from a point charge model using PyCrystalField), the SHG signal is dramatically enhanced compared with non-resonant SHG. Therefore, we can use SHG spectroscopy to precisely determine the CEF level of $CaCo_2TeO_6$. Although this material has inversion symmetry, the electronic dipole SHG is forbidden, the magnetic dipole SHG is allowed. We observed an intense peak around 1.25eV within the energy range in the SHG spectrum, which corresponds to the spin-allowed transition from the $^4T_{2g}$ to $^4T_{1g}$ state. SHG results are consistent with the absorption measurements and provide precise measurements of the CEF energy levels. The energy mismatch between calculated and measured values could arise from the covalency of the Co-O bond that is ignored by the point charge model. We didn't observe significant change in SHG intensity across the magnetic transition temperature ~16 K (4 - 100 K), indicating the origin of the SHG signal was from magnetic dipole or electronic quadrupole.

The calculated dipole moment vector (in arbitrary units):

$$[\ 1.28 \times 10^{-12},\ 7.39 \times 10^{-12},\ -3.82 \times 10^{-12}]$$

Dipole moment magnitude (in arbitrary units):

$$8.42 \times 10^{-12}$$

The calculated quadrupole moment tensor (in arbitrary units):

$$\begin{array}{l} [\,[\ \ 1.35 \times 10^{3}, \quad 1.91 \times 10^{2}, -4.91 \times 10^{3}] \\ \ \ [\ \ 1.91 \times 10^{2}, \quad 6.16 \times 10^{3}, \quad 1.76 \times 10^{3}] \\ \ \ [-4.91 \times 10^{3}, \quad 1.76 \times 10^{3}, \quad 7.51 \times 10^{3}]\,] \end{array}$$

Principal components of the quadrupole moment tensor:

$$[-6.56 \times 10^{3},\ -3.28 \times 10^{3},\ 9.84 \times 10^{3}]$$

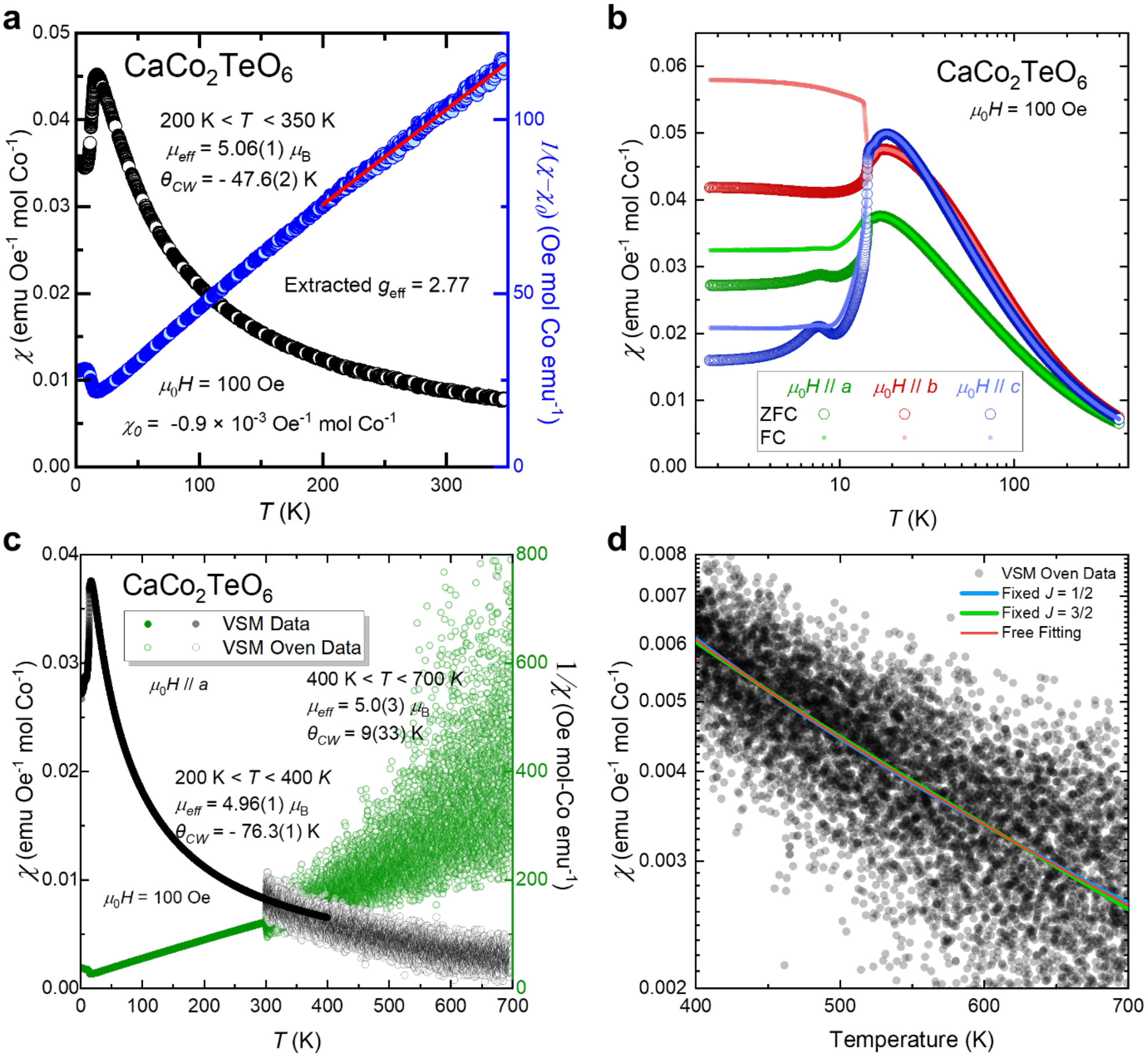

Figure S4. (a) Magnetic susceptibility from powder. (b) Orientation-dependent magnetic susceptibility as a function of temperature (c) High-temperature magnetic susceptibility. (d) Fittings on high-temperature magnetic susceptibility.

Fitted result from Fig. S4d:

Fitting Type	θ_{CW}	μ_{eff}	χ_0	R^2
Fixed $J = 1/2$	36(2)	4.47 (Fixed, $S = 3/2$, $L = 1$)	-0.00161(3)	0.61179
Fixed $J = 3/2$	-58(3)	5.67 (Fixed, $S = 3/2$, $L = 2$)	-0.00273(3)	0.61165
Free Fitting	9(33)	5.01(3)	-0.00194(4)	0.61178

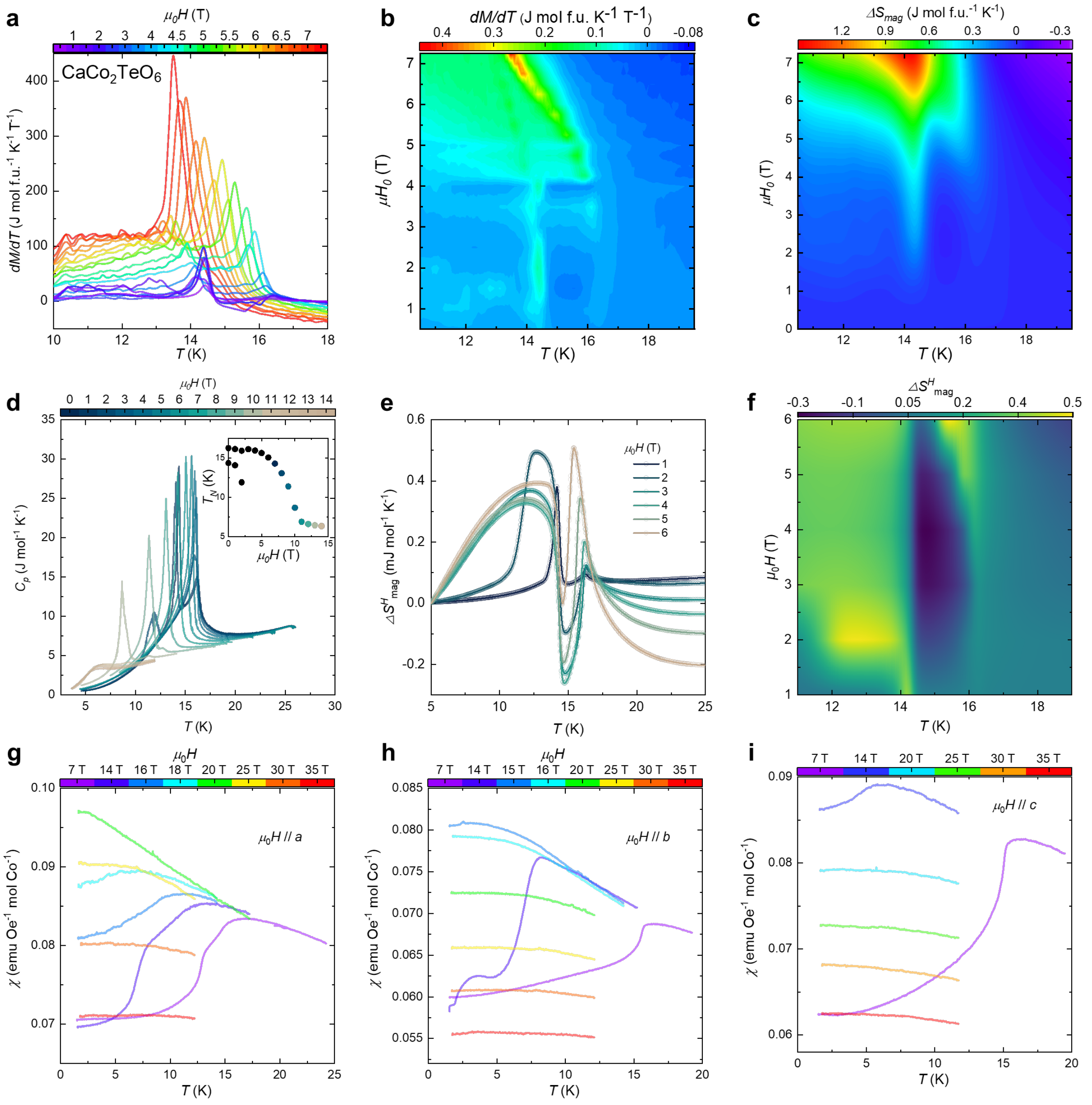

Figure S5. (a) First derivative of magnetization with respect to temperature under magnetic field. (b) A map of dM/dT = dS/dH showing two magnetic transitions. (c) A magnetic entropy map. (d) Field dependent heat capacity. (e, f) magnetic entropy change with respect to field extracted from heat capacity. (g-i) Temperature dependent magnetic susceptibility along different directions under high magnetic field.

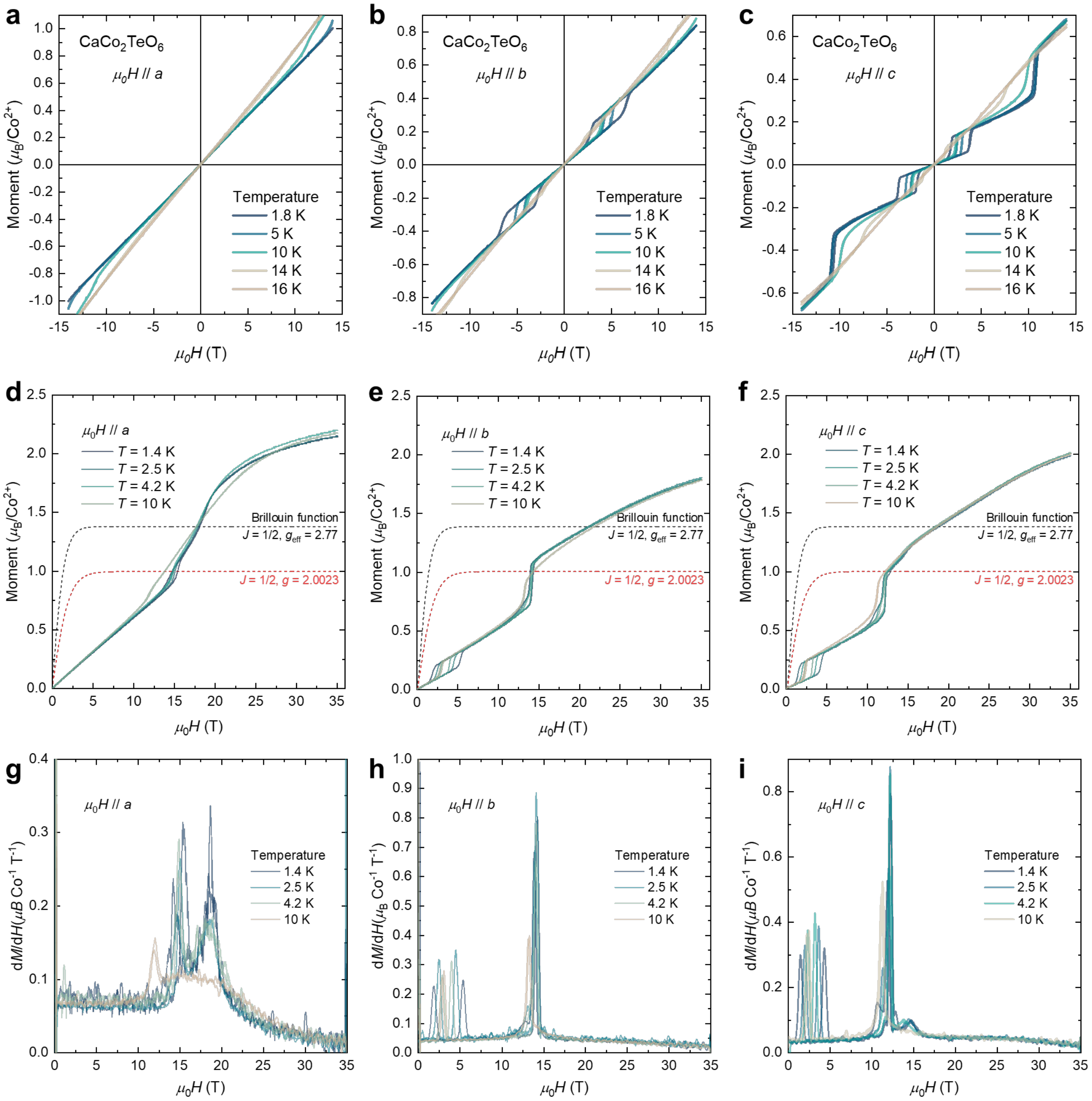

Figure S6. Orientation-dependent magnetization under magnetic field up to 35 T.

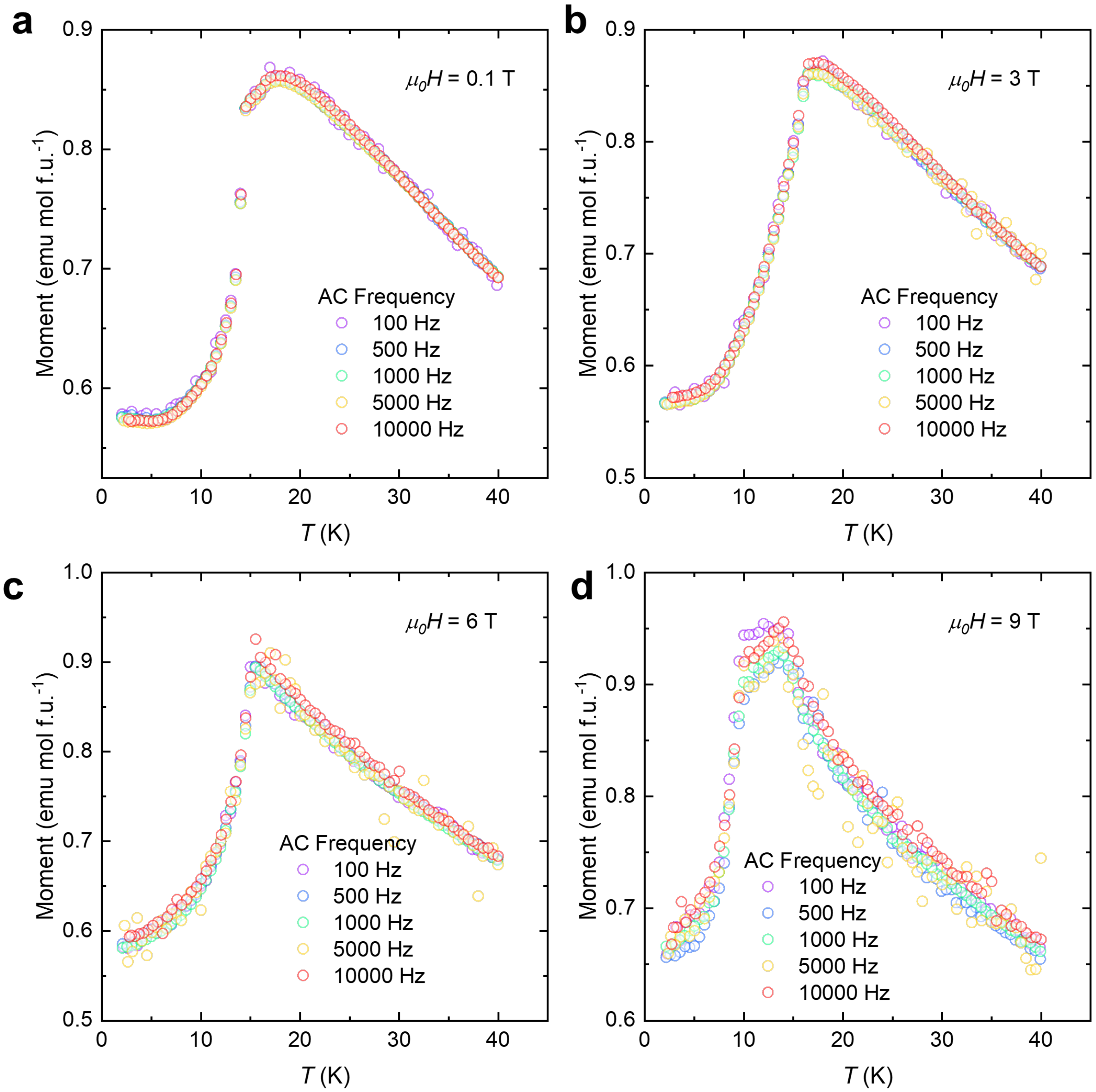

Figure S7. AC magnetization at around transition temperature under different frequency.

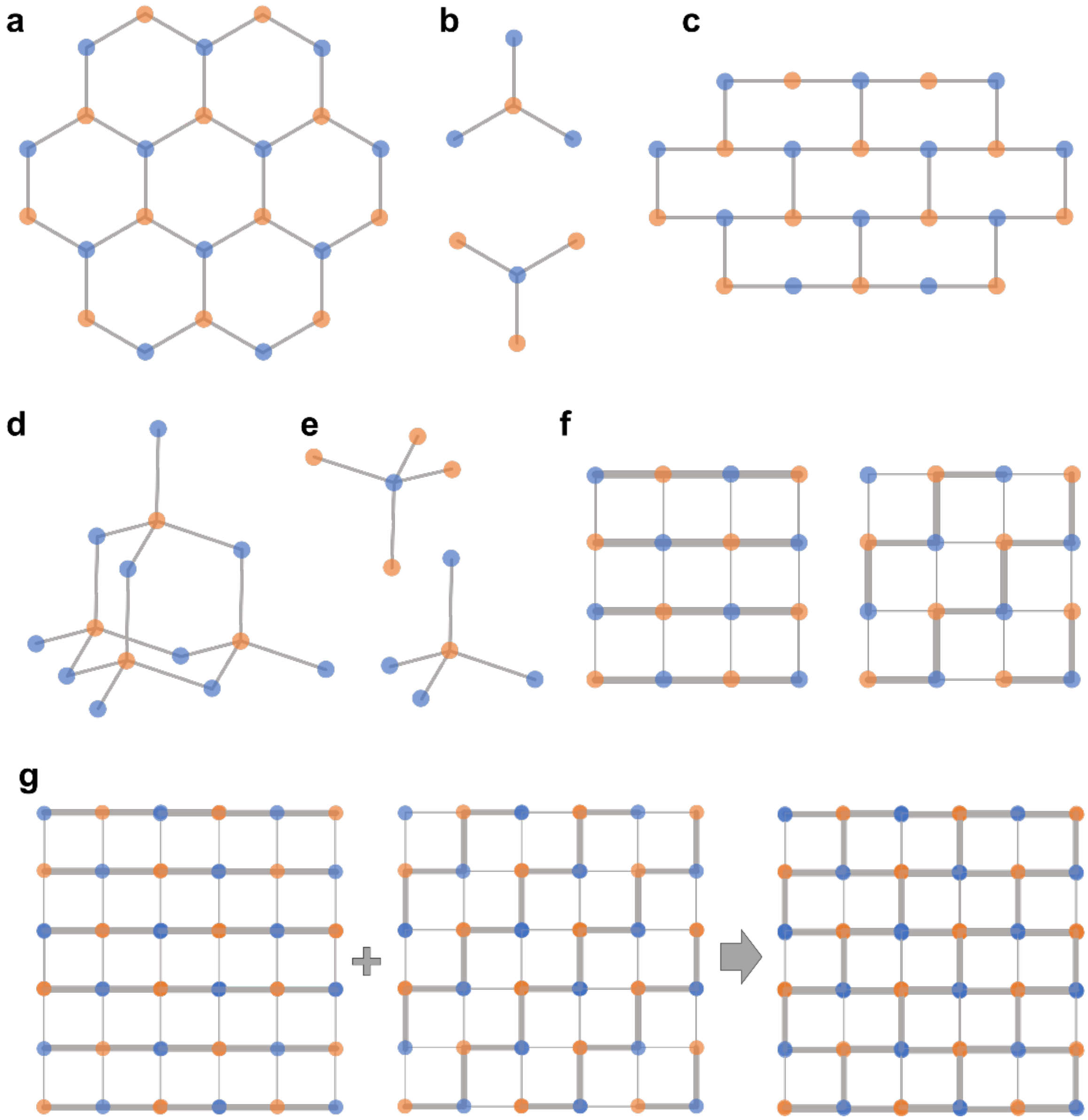

Figure S8. Comparison between honeycomb and diamond lattice.

The honeycomb lattice (a) and diamond lattice (d) are both bipartite lattices where the lattice is composed of two different sites, as shown in (b) and (e), and both features competing nearest-neighbor (between different sites) and second nearest-neighbor interactions (between same sites). When we pull the honeycomb lattice horizontally, the interactions in the honeycomb lattice can be illustrated as rectangular blocks with the strongest nearest-neighbor interactions highlighted in gray (c). When the diamond lattice is pressed into 2D, it forms a squire net, as shown in (f). In the $CaCo_2TeO_6$ case, among the four nearest neighbors, two of the Co-Co interactions are stronger (highlighted as bold gray lines) than the other due to different exchange interaction pathways. Due to the reduction of dimension, the 3-D diamond lattice shows both types of interactions as illustrated in (g), resulting in a honeycomb-like (approximate Kitaev) interaction.

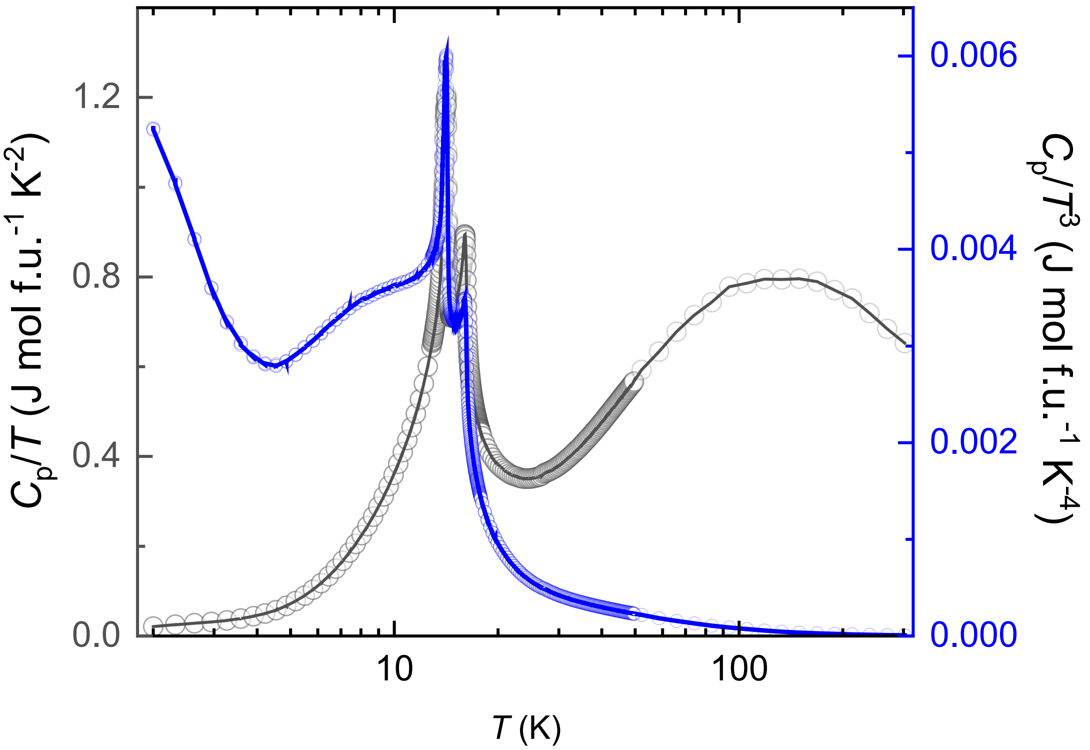

Figure S9. C_p/T and C_p/T^3 as a function of temperature, showing the presence of Einstein mode phonon.

Extracting the magnetic contribution to the heat capacity requires a reliable phonon subtraction using a most direct nonmagnetic isostructural analog or a phonon model. We attempted to prepare the unknown $CaZn_2TeO_6$ as the nonmagnetic version for subtracting the lattice contribution, but were not successful. Thus, we constructed a phonon model that best describes the high-temperature heat capacity data by using two Debye modes and one Einstein model.

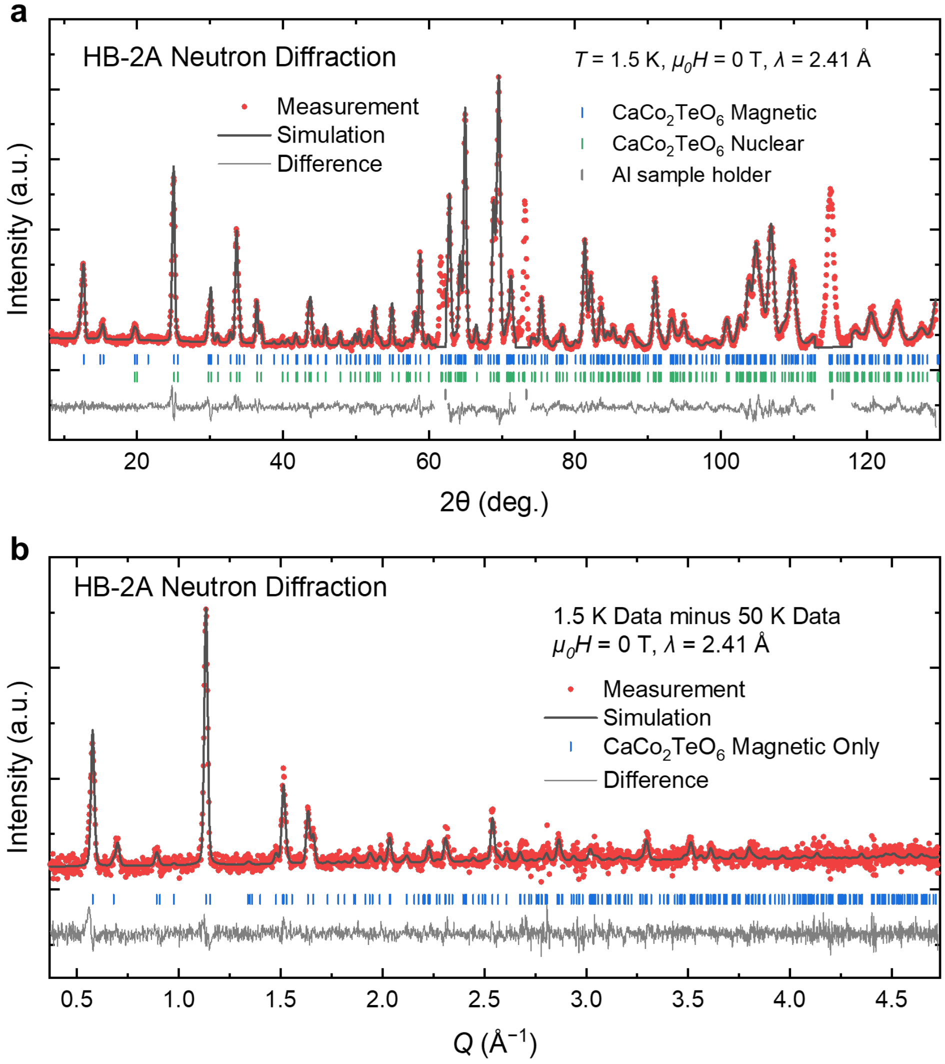

Figure S10. HB-2A Powder neutron diffraction.

The magnetic structure was fitted with all maximal magnetic space groups (As shown in the table below). The *Pnma* (62.441) shows the best agreement in terms of peak position and intensity.

MSG	**# Parameters**	**R_{WP}**	χ^2
Pnma (62.441)	6	15.5	2.871
Pn’ma (62.443)	6	26.8	7.789
Pnm’a (62.444)	6	26.1	7.356
Pnma’ (62.445)	6	19.1	3.968
Pn’m’a (62.446)	6	27.7	8.315
Pnm’a’ (62.447)	6	22.6	5.515
Pn’ma’ (62.448)	6	23.7	6.069
Pn’m’a’ (62.449)	6	25.5	7.021

The magnetic vectors were initially allowed to refine freely, and the result shows a small value and large error for M_x , indicating the M_x parameters are not well constrained.

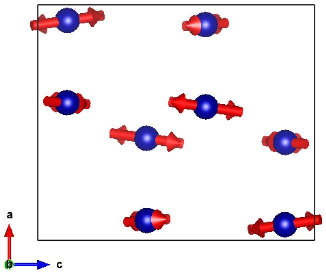

Co	M_x	M_y	M_z	M_{tot}
Co(1)	-0.412(96)	-1.040(72)	2.863(26)	3.07
Co(2)	-0.130(100)	1.373(71)	1.644(27)	2.16

Then we tried to set the magnetic moment to zero.

Co	M_x	M_y	M_z	M_{tot}
Co(1)	0 (Fixed)	-1.045(74)	2.862(26)	3.04
Co(2)	-0.477(84)	1.371(73)	1.663(27)	2.21

Co	M_x	M_y	M_z	M_{tot}
Co(1)	-0.458(77)	-1.072(85)	2.863(26)	3.09
Co(2)	0 (Fixed)	1.345(84)	1.659(27)	2.14

And if both are fixed to 0:

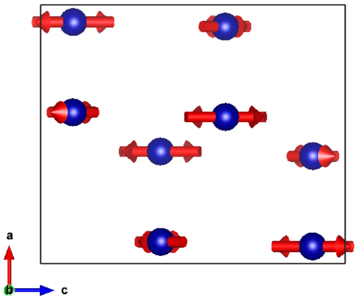

Co	M_x	M_y	M_z	M_{tot}
Co(1)	0 (Fixed)	-0.91(1)	2.07(2)	2.3(1)
Co(2)	0 (Fixed)	0.91(1)	1.16(1)	1.4(1)

The diffraction data still fit well (Figure S22). Overall, slight canting out of the *bc*-plane can be included without affecting the fit drastically.

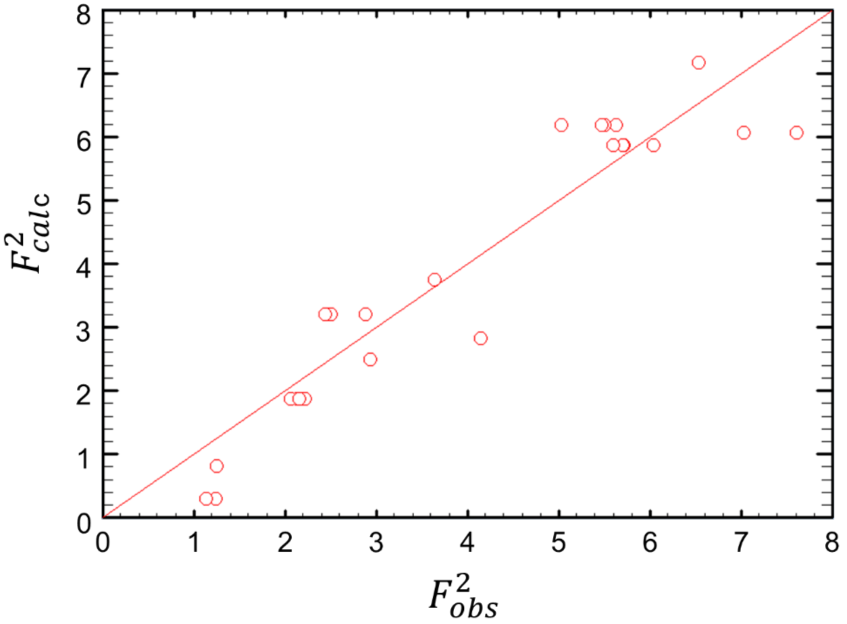

Figure S11. The observed magnetic squared structure factors vs. calculated from the FullProf refinement from CORELLI data.

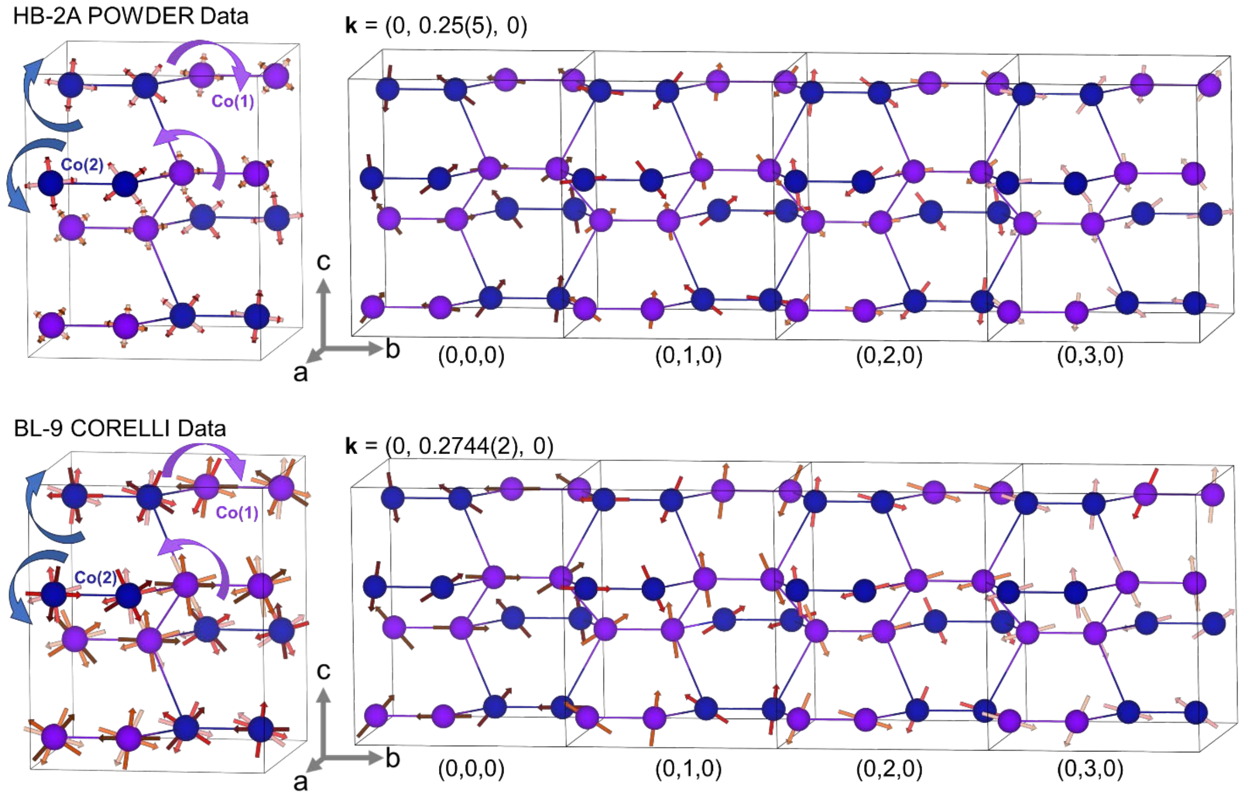

Figure S12. Magnetic structure at 15 K from HB-2A powder neutron diffraction and BL-9 single crystal neutron diffraction at 14.5 K.

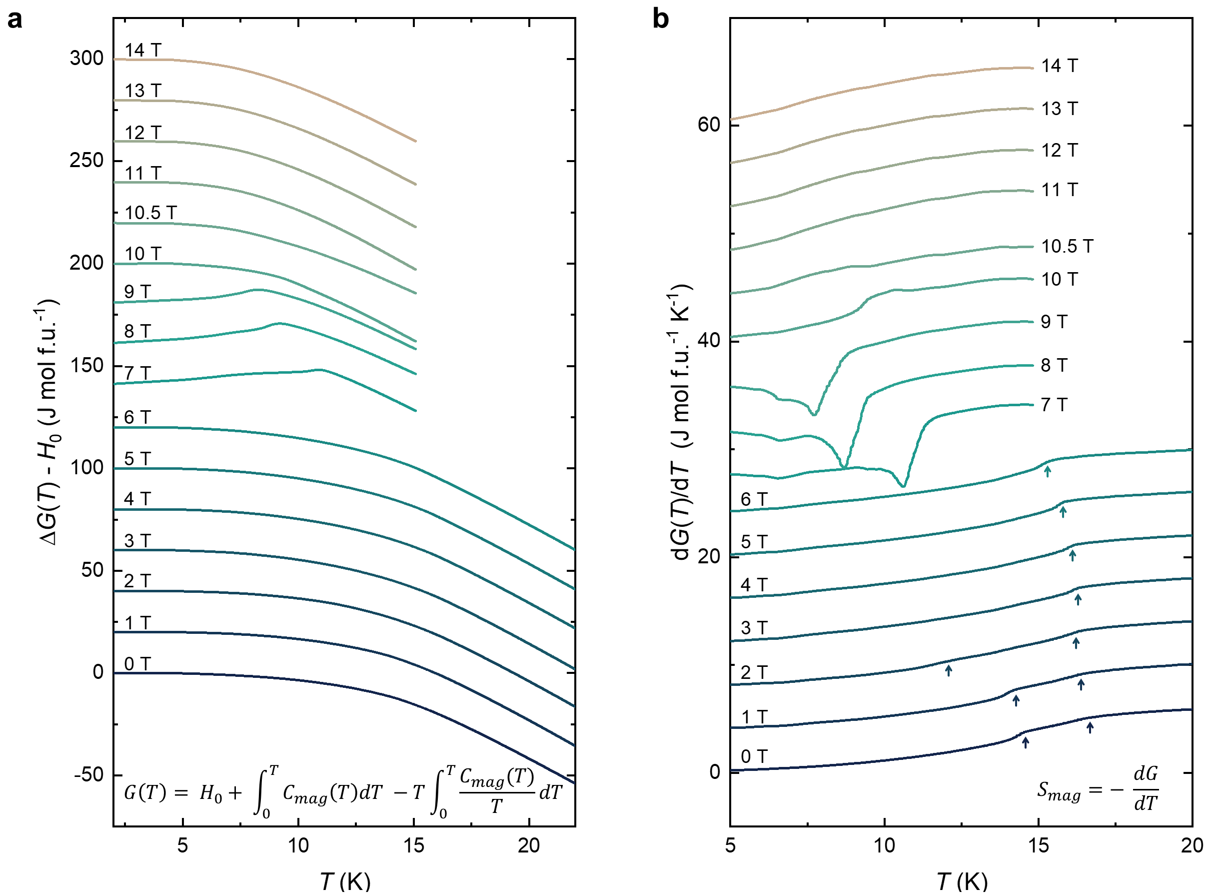

Figure S13. Magnetic Gibbs free energy and entropy as a function of temperature and magnetic field. (a) $\Delta G(T)-H_0$ obtained from $C_{\mathrm{mag}}(T)$ data. (b) Magnetic entropy $S_{\mathrm{mag}} = -\mathrm{d}G/\mathrm{d}T$.

To improve visibility, a constant vertical offset of +20 J mol^{-1} was added sequentially to the Gibbs free energy curves for each higher-field dataset relative to the previous one, with the 0 T curve remaining unshifted. Similarly, a vertical offset of +4 J mol^{-1} K^{-1} was applied sequentially to the d$G(T)$/dT curves between adjacent fields to enhance clarity.

To better understand *the nature* of the transitions presented in Fig 5h, we evaluated the magnetic Gibbs free energy and its temperature derivative, which corresponds to magnetic entropy (Fig. S13). Below 6 T, the entropy curves exhibit slight discontinuities and downward-bending features, and characteristic jump in entropy of first-order transitions associated with the PM → I-AFM → NC-AFM sequence. From 7 T to 10.5 T, the transitions remain first order, though the system no longer passes through the I-AFM state. In this field range, the unusual curvature in the entropy reflects proximity to a triple point where PM, spin-flop AFM (SF-AFM), and I-AFM phases intersect. The latent heat associated with the first order transition features are also shown in the heat curve (Fig. S14) as shoulders in the curve at $\mu_0 H \leq 10.5$ T. While at above 11 T, the entropy evolves smoothly and bends upward (Fig. S13), and the heat curve shows absence of latent heat, indicating a crossover to second-order behavior as the system enters a quantum paramagnetic (QPM) phase. These findings are consistent with the metamagnetic transitions and enhanced entropy observed in magnetization and heat capacity data (Figs. 2e,f and S7).

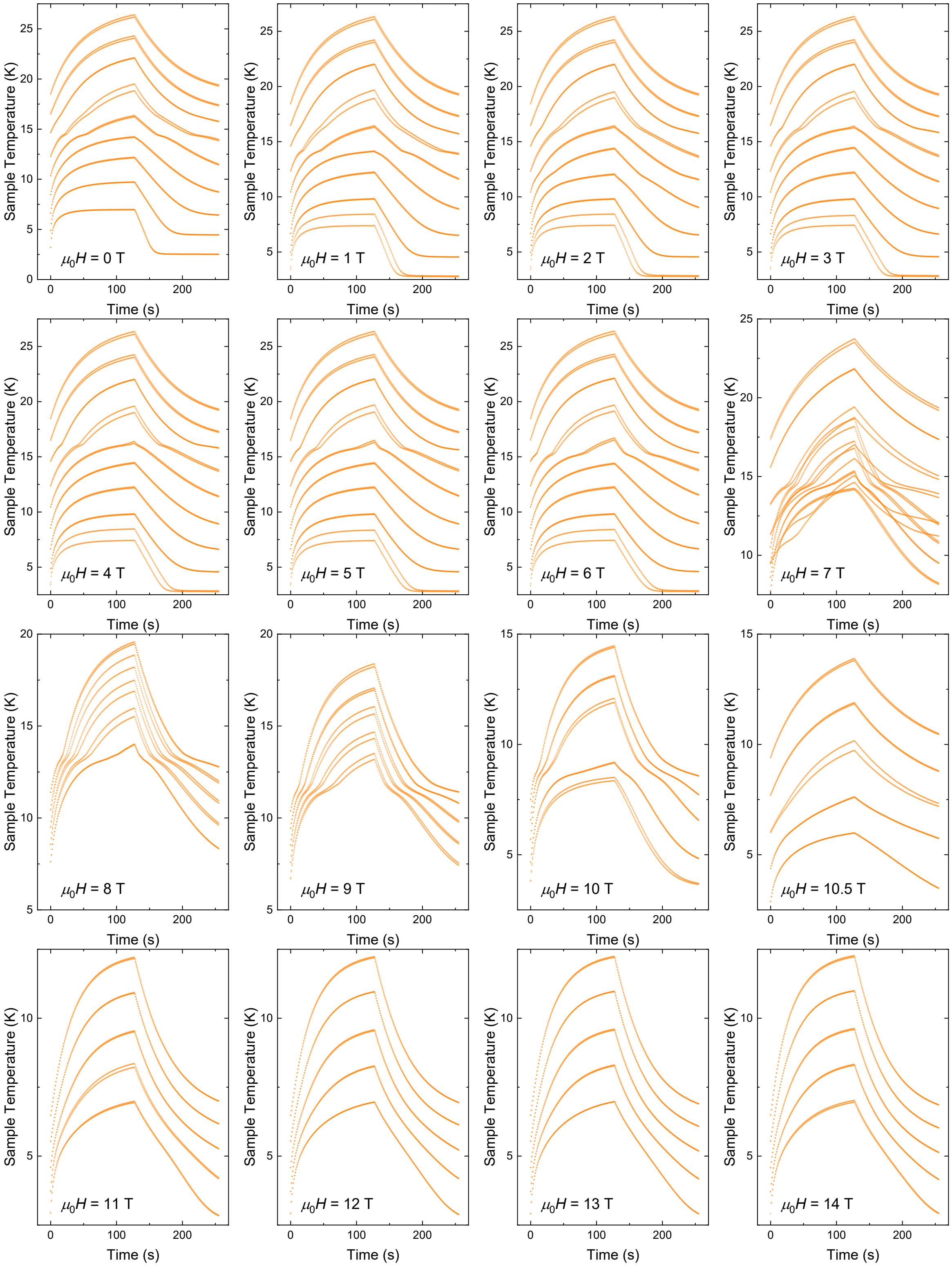

Figure S14. Heat curves from temperature dependent heat capacity measurements under fields.

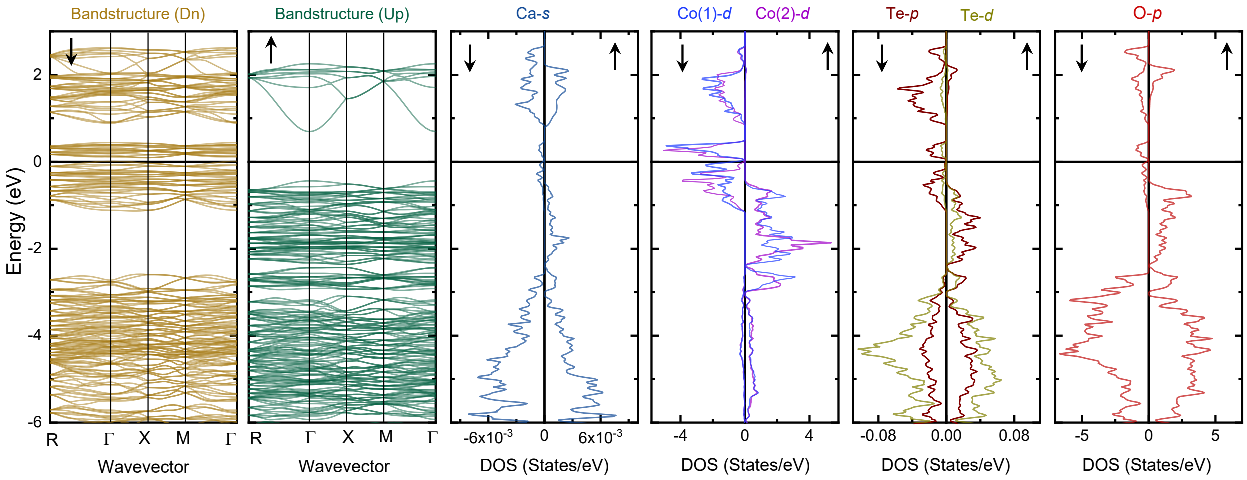

Figure S15. FP-LAPW band structure and DOS of $CaCo_2TeO_6$.

To connect the quantum-mechanical interference phenomena to the uniqueness of $CaCo_2TeO_6$ full-potential linearized augmented plane-wave (FP-LAPW) spin-polarized DFT calculations were performed (Fig. S15). The bands around the Fermi level (E_F) are diffused, indicating covalent characters and appreciable overlap between the Co-*d* and O-*p* states. The spins of the Co-*d* states are polarized and further polarize the O-*p*, Te-*s*/*p*, and Ca-*s* states, suggesting Heisenberg magnetic interactions along different directions. The valence band maximum and conduction band minimum primarily consist of the Co-*d* and O-*p* states. This indicates sizable Co-O-Co interactions, facilitating magnetic exchange pathways. The DFT results underscore the rich magnetic behavior of $CaCo_2TeO_6$ while appreciating the presence of competing nearest-neighbor and next-nearest-neighbor magnetic exchange interactions.

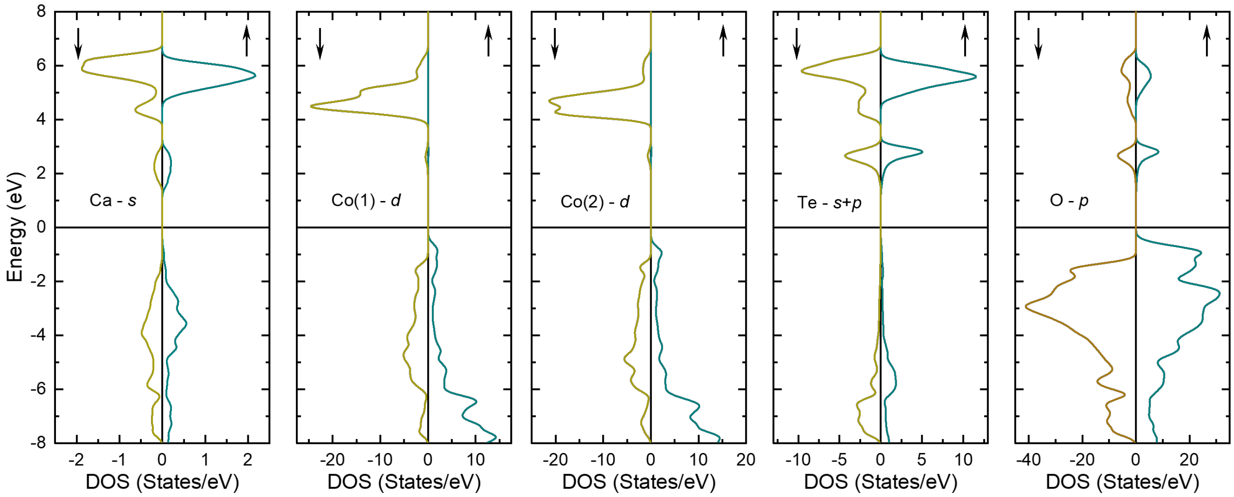

Figure S16. DOS of $CaCo_2TeO_6$ calculated using the PAW method.

Additional plane-wave DFT calculations were performed by utilizing the projector-augmented wave (PAW) method and projected into a linear combination of atomic orbital (LCAO). The spin-polarized DOS curves from the pseudopotential calculations are similar to those from FP-LAPW validating the DFT results.

To compare the overlap of the atomic interacting wavefunctions and the electronic instability of T_d-[CoO_4] in $CoRh_2O_4$ vs. O_h-[CoO_6] in $CaCo_2TeO_6$, we extracted the projected crystal orbital Hamilton population (-pCOHP) and integrated the COHP (ICOHP) of the Co-*d* and O-*p* orbitals within each O_h-[CoO_6] and T_d-[CoO_4] cluster up to E_F per unit cell (Fig S16-21).

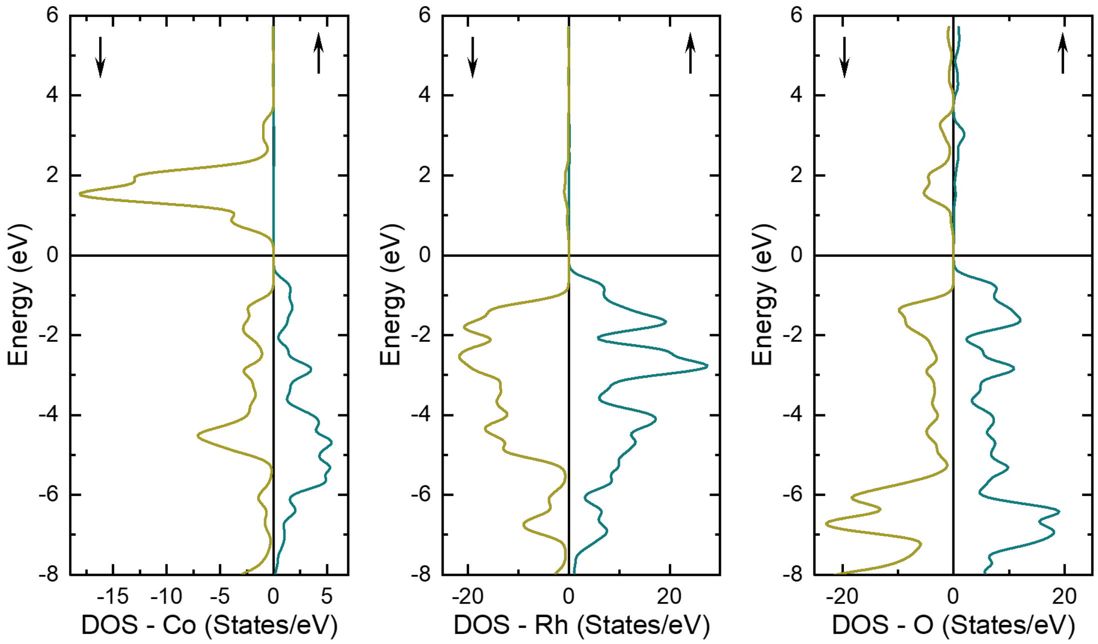

Figure S17. DOS of $CoRh_2O_4$ calculated using the PAW method.

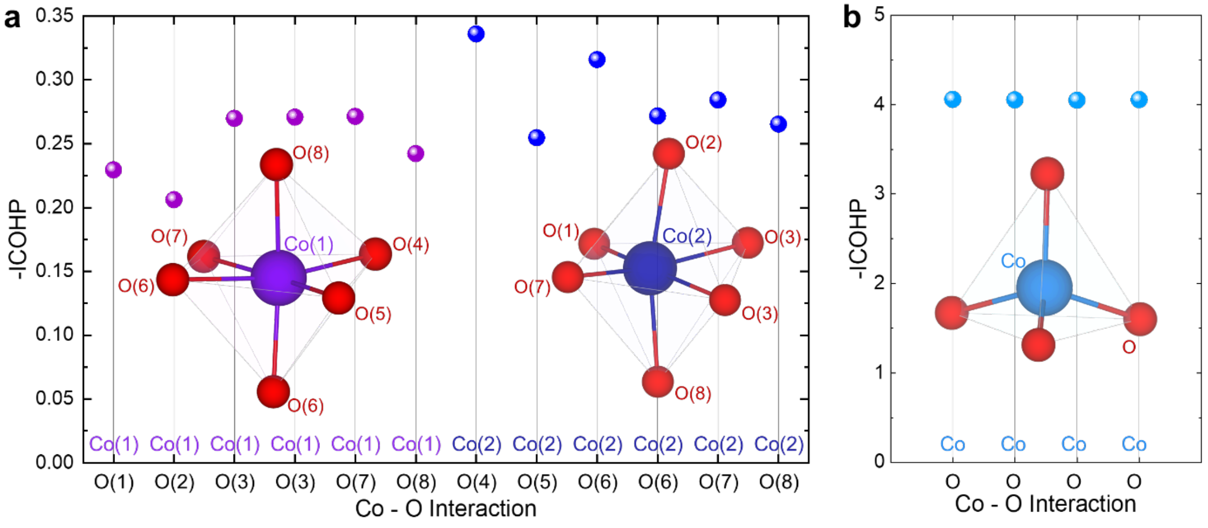

Figure S18. Crystal orbital Hamilton population and integration for Co-O bonds in (a) $CaCo_2TeO_6$ and (b) $CoRh_2O_6$.

The total integrated Co-O COHPs up to E_F (ICOHPs) show overall bonding strength for O_h-[CoO_6] in $CaCo_2TeO_6$ and T_d-[CoO_4] in $CoRh_2O_4$. For O_h-[CoO_6], the total Co-O interaction strengths are similar in magnitude, and overall, the Co(1)-O bonds are slightly stronger than the Co(2)-O bonds. For T_d-[CoO_4], the Co-O bonds feature the same strength due to symmetry.

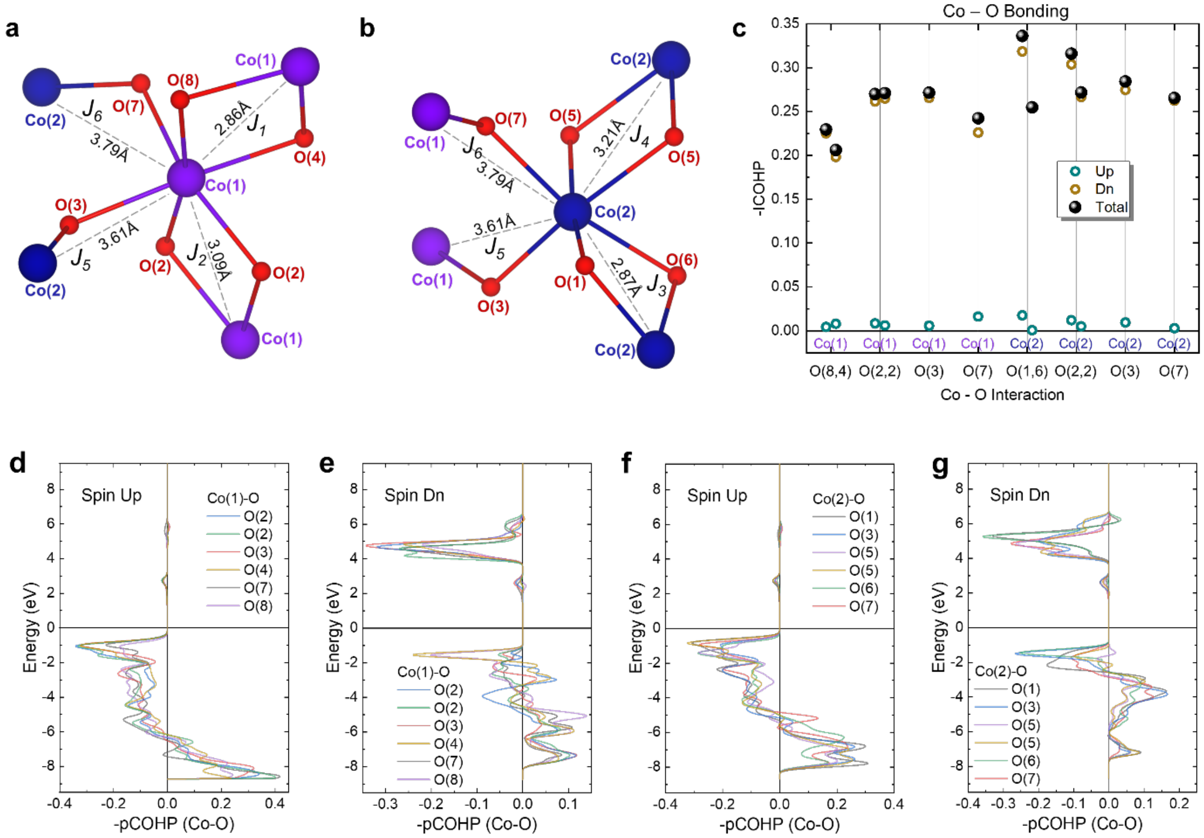

Figure S19. Crystal orbital Hamilton population and integration for Co-O bonds in $CaCo_2TeO_6$. The -pCOHP curves for O_h-[CoO_6] shows Co-O antibonding characters, as proposed in Fig. S1.

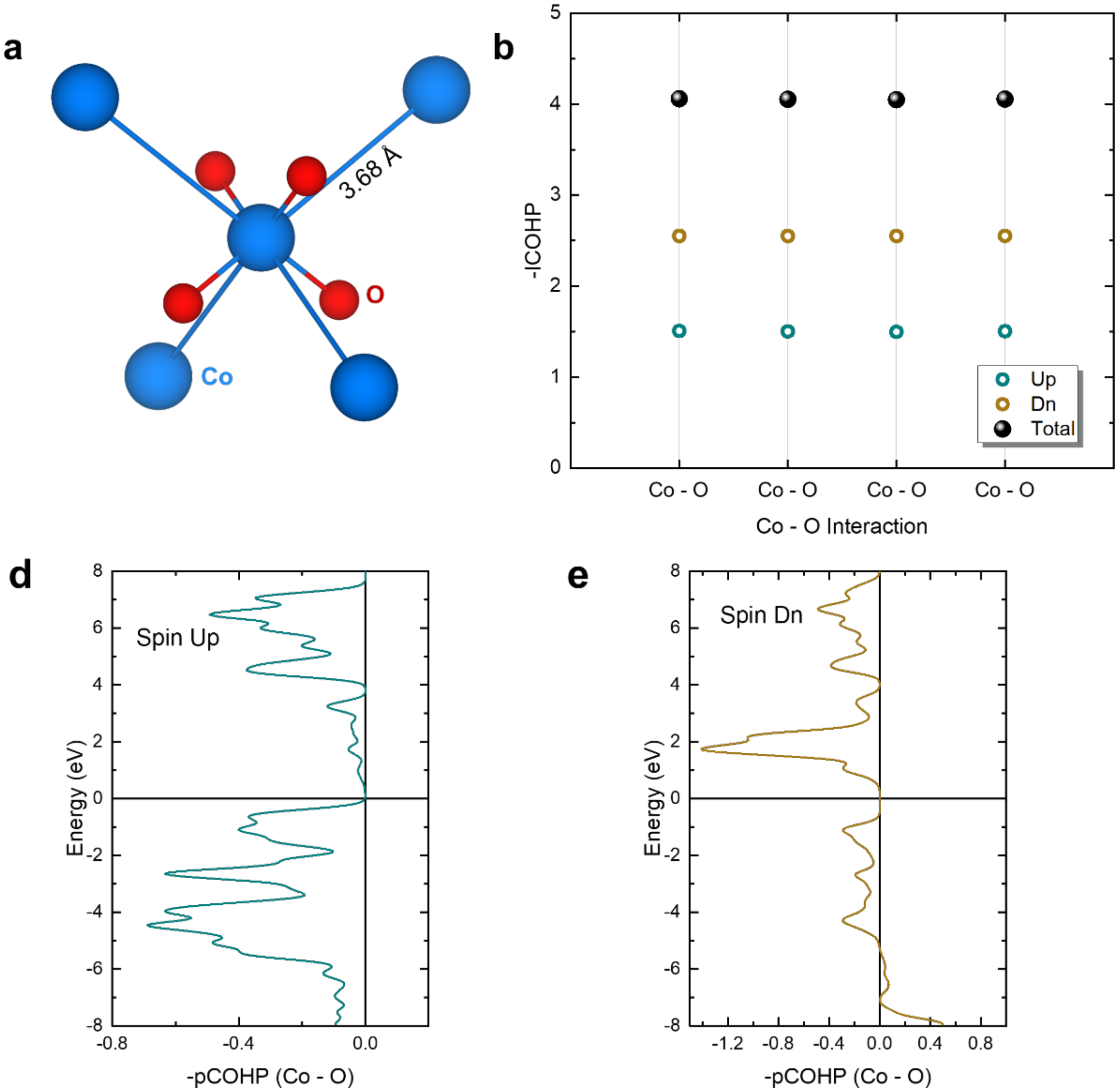

Figure S20. Crystal orbital Hamilton population and integration for Co-O bonds in $CoRh_2O_6$. The -pCOHP curves for T_d-[CoO_4] also shows Co-O antibonding characters.

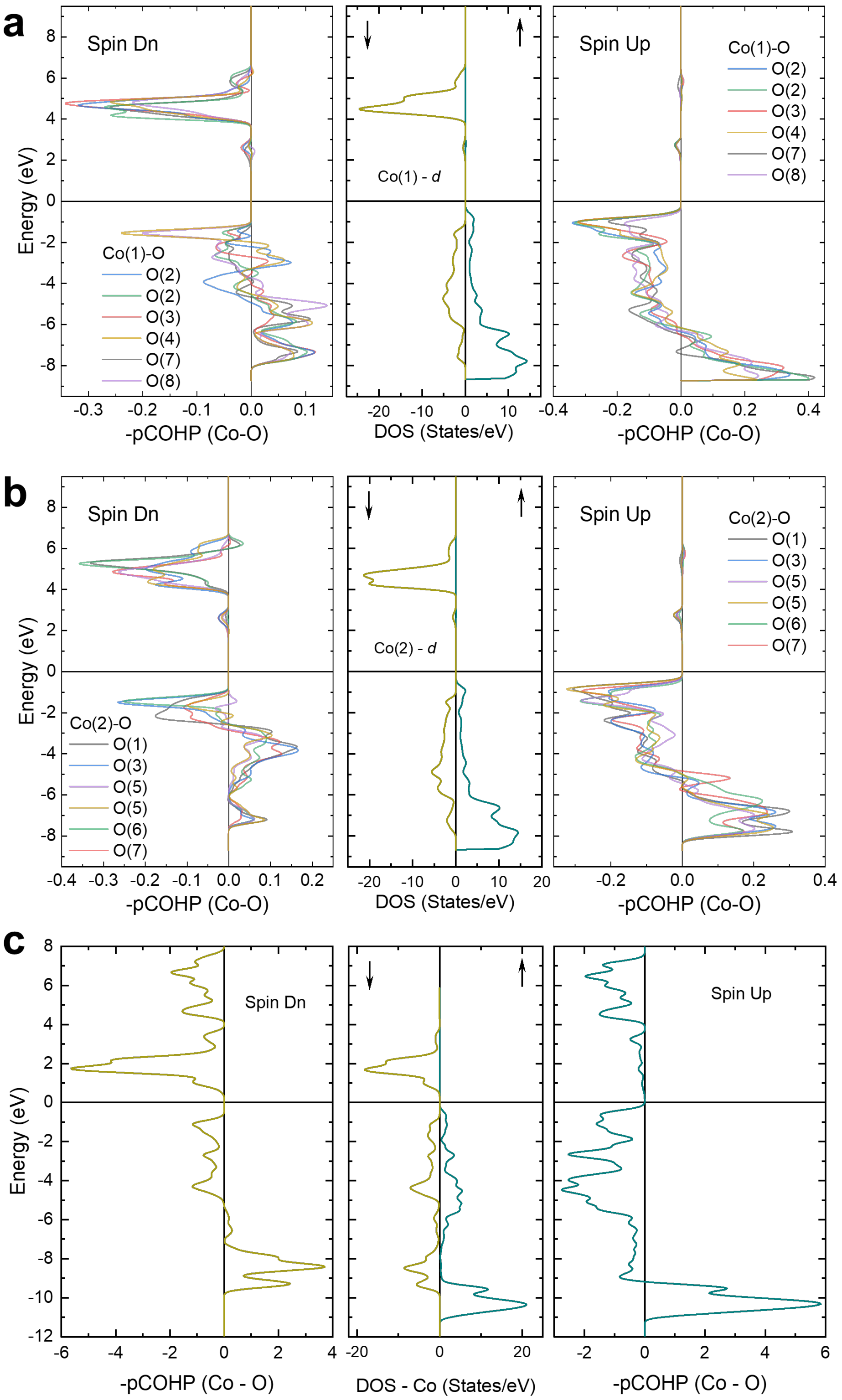

Figure S21. DOS of Co-*d* and pCOHP.
The energy scale integrated in Fig. 5a, b is determined from the DOS curve.

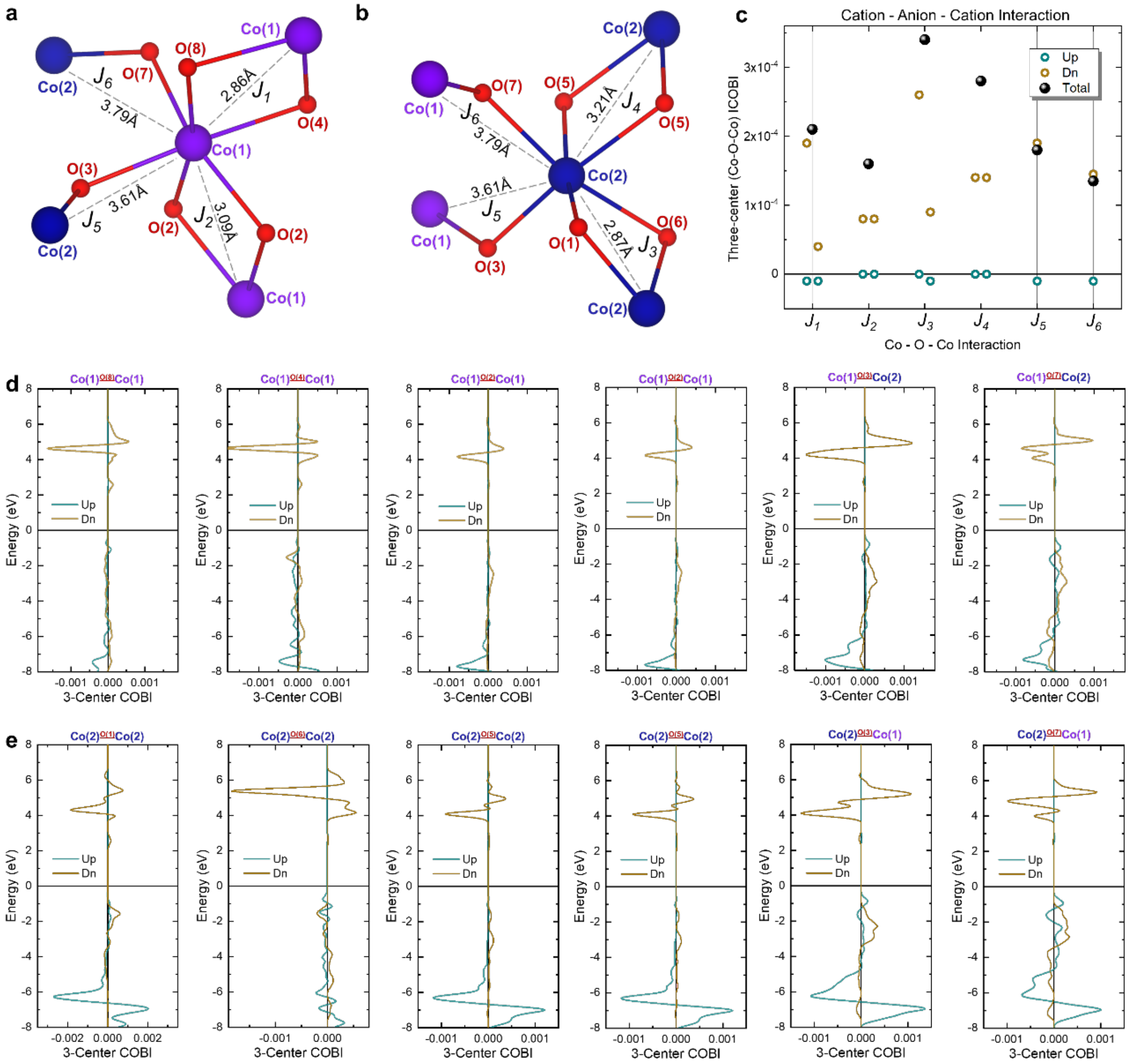

Figure S22. Crystal Orbital Bond Index for Co-O-Co bonds in $CaCo_2TeO_6$.

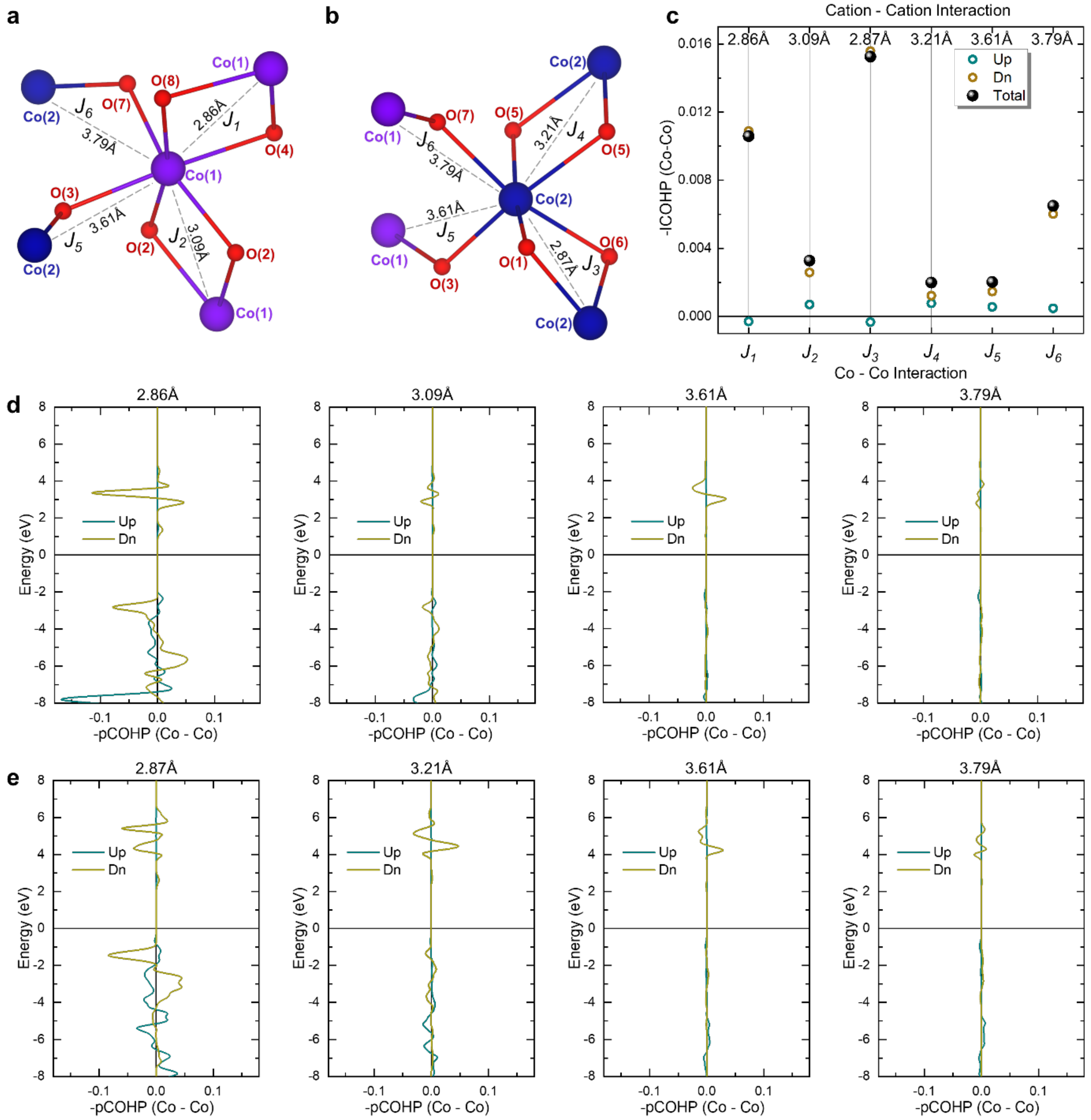

Figure S23. Crystal orbital Hamilton population and integration for Co-Co interactions in $CaCo_2TeO_6$.

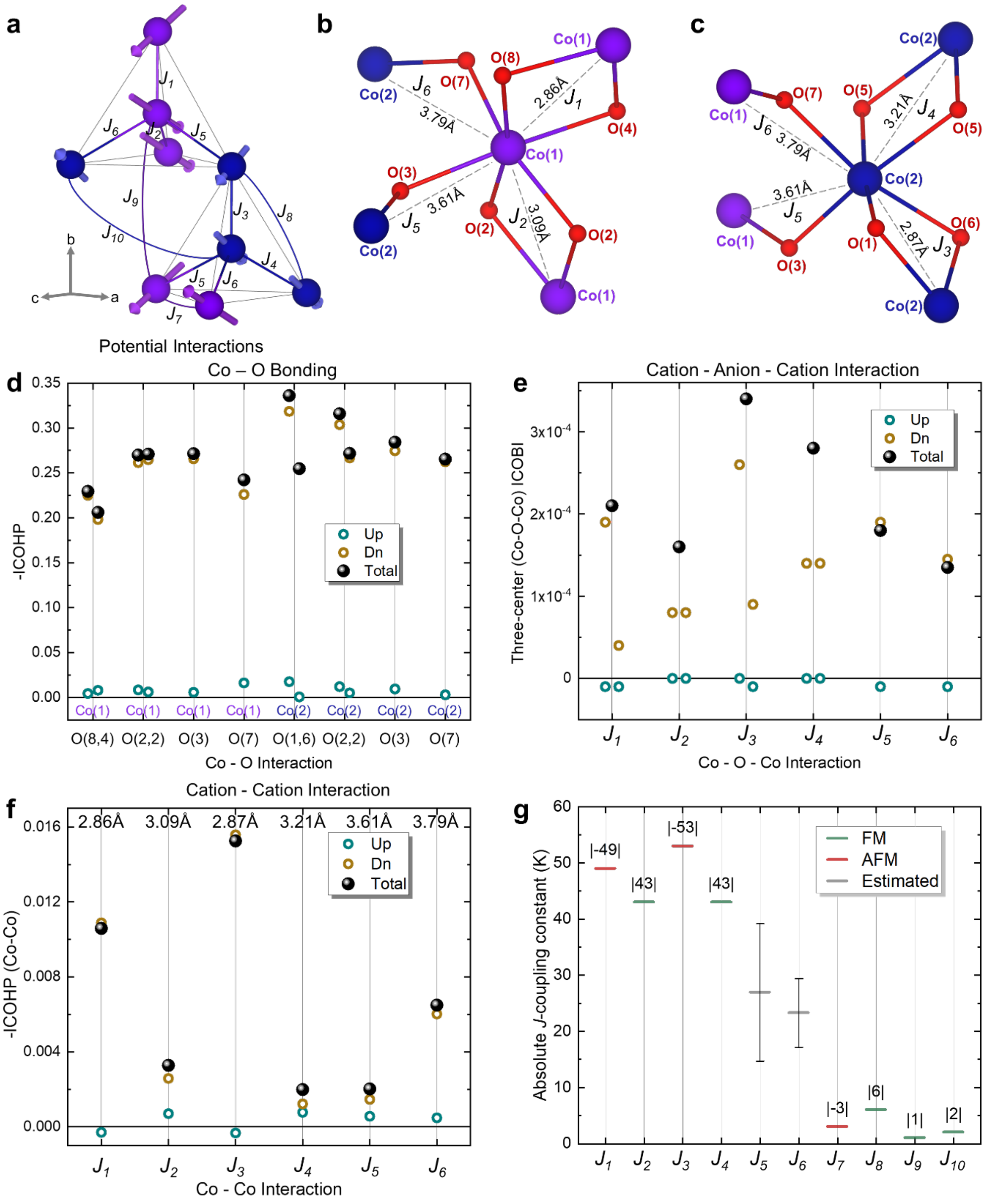

Figure S24. Interactions in $CaCo_2TeO_6$.

The three-center COBI curves (Fig. S22) between same pairs of Co atoms (e.g. $\text{Co(1)}\overset{\text{O(8,4)}}{\overline{\qquad}}\text{Co(1)}$ and $\text{Co(2)}\overset{\text{O(1,6)}}{\overline{\qquad}}\text{Co(2)}$ curves) show similar features that confirmed that the bond strength between Co and O are comparable. And the integration (ICOBI) (Fig. S22c) implies that interactions between identical Co types ($J_{1\text{-}4}$, facilitated through two Co-O-Co pathways: $\text{Co(1)}\overset{\text{O(8,4; 2,2)}}{\overline{\qquad}}\text{Co(1)}$, $\text{Co(2)}\overset{\text{O(1,6; 5,5)}}{\overline{\qquad}}\text{Co(2)}$) surpass those between different Co types ($J_{5,6}$, mediated by a singular O bridge: Co(1)$\overset{\mathrm{O(3)}}{\text{——}}$Co(2), Co(1)$\overset{\mathrm{O(7)}}{\text{——}}$Co(2)). Consistent with the ICOHP, the cation-anion-cation interaction between Co(2) is still stronger than that for Co(1). Although the total ICOBI between Co(1)$\overset{\mathrm{O(2,2)}}{\text{——}}$Co(1) and Co(1)$\overset{\mathrm{O(3)}}{\text{——}}$Co(2) appears identical, the 3-center ICOBI only take the cation - anion – cation (e_g – p - e_g) into account, ignoring the direct cation-cation (t_{2g} - t_{2g}) interaction between edge-shared Co atoms.[12, 13] To quantify the direct interactions between the same type of Co, we calculated the COHP between Co in the shown cluster (Fig. S23). The ICOHP (Fig. S23f) confirmed that the interaction between Co(1)-Co(1) (3.09Å) is stronger than that of Co(1)-Co(2) (3.61Å). Moreover, if we take a closer look at the cation-cation interaction, the Co(1)$\overset{\mathrm{O(8,4)}}{\text{——}}$Co(1) and Co(2)$\overset{\mathrm{O(1,6)}}{\text{——}}$Co(2) interactions are a lot stronger than that in Co(1)$\overset{\mathrm{O(2,2)}}{\text{——}}$Co(1) and Co(2)$\overset{\mathrm{O(5,5)}}{\text{——}}$Co(2) although they both form edge sharing octahedra. This is most likely due to the local environment difference (Fig. S25a). Take Co(1) as an example, the bonds between Co(1)-O(4)-Co(1)-O(8) are perpendicular to the *d*-z^2 orbital, while the Co(1)-O(2)-Co(1)-O(2) bonds are distorted due to crystal field splitting and deviate from the *d*-z^2 orbital, so the *d*-e_g orbitals of Co(1)$\overset{\mathrm{O(2,2)}}{\text{——}}$Co(1) are pointing at similar direction but different layer, resulting in less overlap. This direct cation-cation interactions can be confirmed from the DOS curve of decomposed *d*-t_{2g} orbitals (Fig. S25b,c), that the *d*-yz and *d*-xz orbital in spin up, *d*-xy and *d*-xz in spin down states from Co(1), and *d*-xy and *d*-xz in spin up, *d*-yz and *d*-xz orbital in spin down states from Co(2) falls to similar trends. In addition, the Co(1)-Co(2) (3.61Å) interaction is weaker than Co(1)-Co(2) (3.79Å) interaction even though the atomic distance is closer. This could be arisen from the potential e_g-e_g interaction between different types of Co (Fig. S26a), where the Co(1)-O(7)-Co(2) bond angle ($127.9(1)^{\circ}$) is closer to 180° than Co(1)-O(3)-Co(2) ($119.2(1)^{\circ}$). Indicating that the *d*-e_g orbitals of site d and e are pointing at similar directions. The decomposed *d*-e_g orbitals (Fig. S26b, c) confirmed this hypothesis that the *d*-z^2 and *d*-x^2-y^2 orbitals from different Co sites follows the same trends.

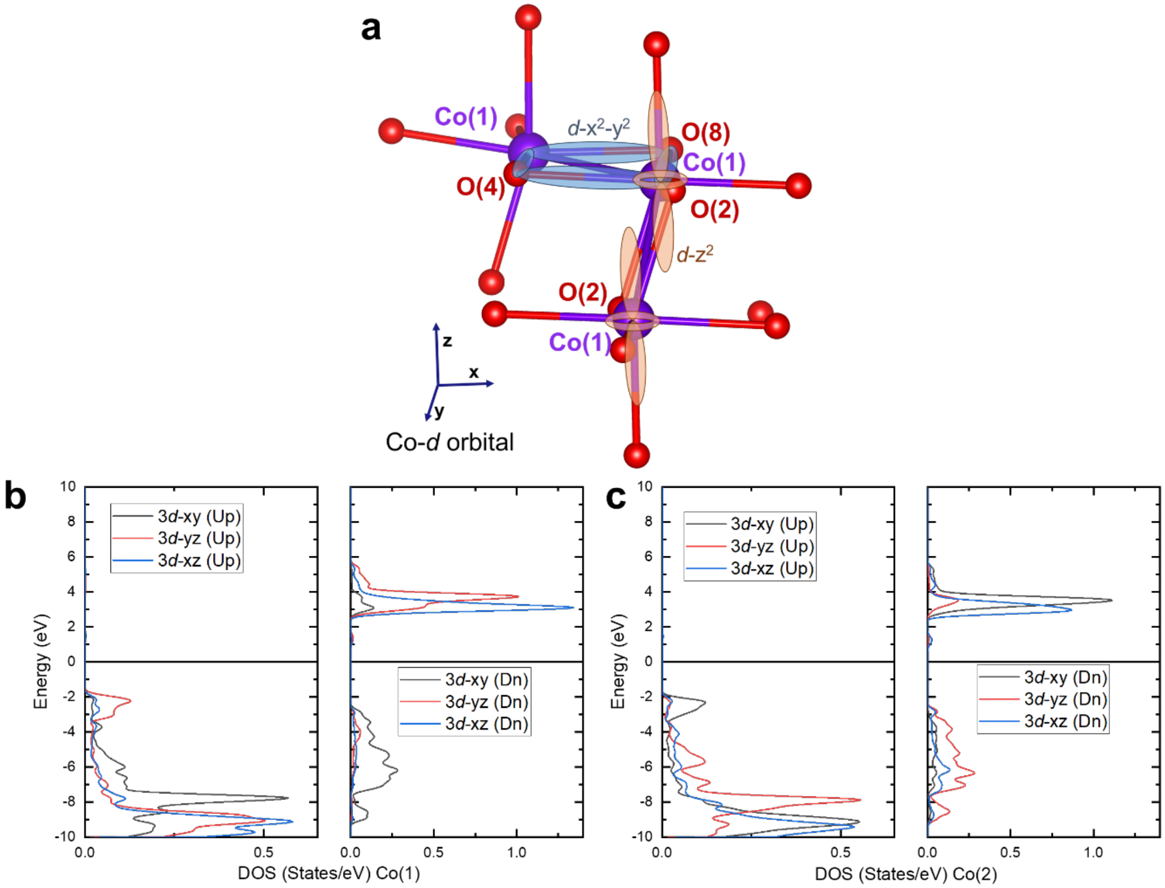

Figure S25. Local environment in Co(1)-centered tetrahedra between same type of Co.

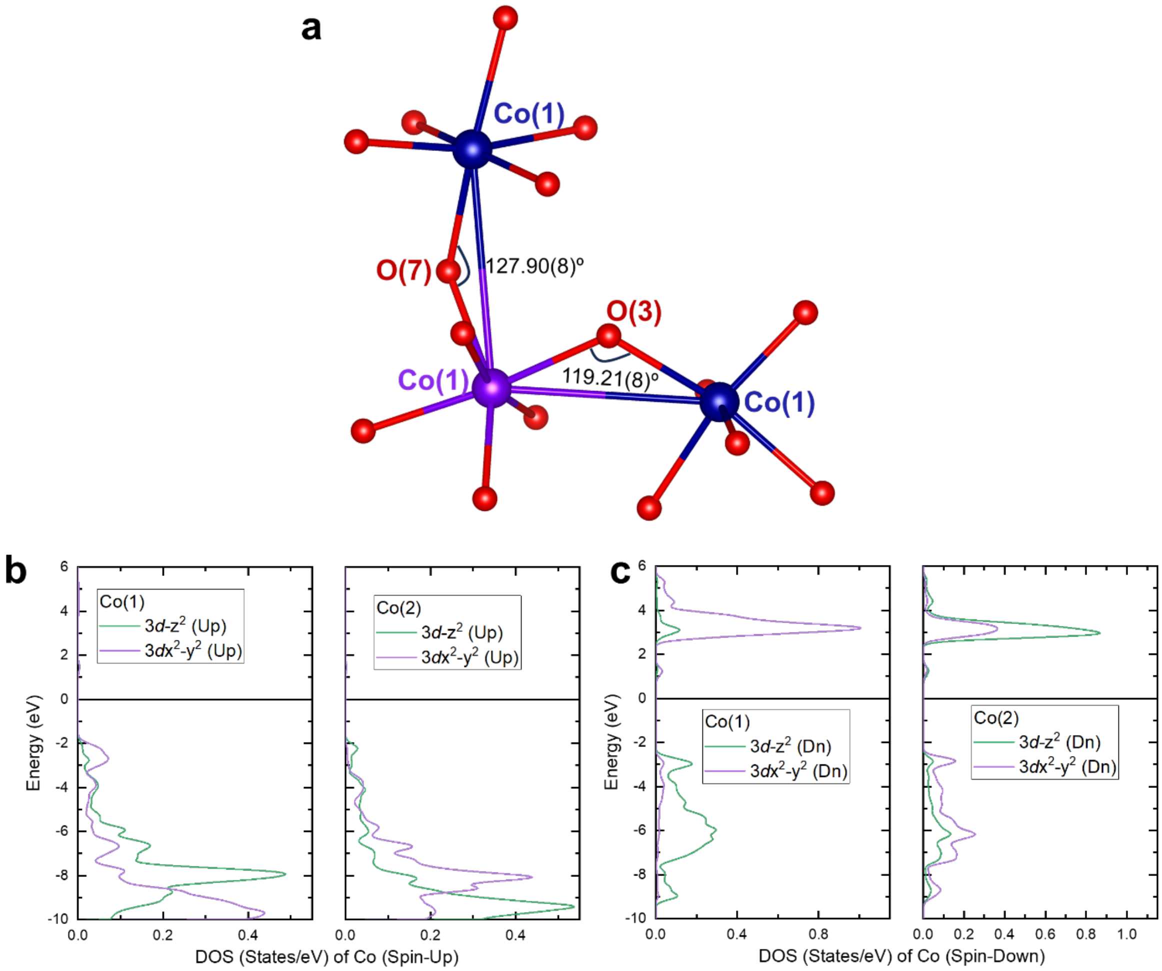

Figure S26. Local environment in Co(1)-centered tetrahedra between different types of Co.

Table S1. $CaCo_2TeO_6$ and compounds with similar magnetic structure.

Compound	**Space Group**	**T_N (K)**	**Magnetic ground state**	**Observed Moment (µB)**	**Expected Moment (µB)**	**Moment Recovery (%)**	**Reason for reduction**
$MnSc_2S_4$ [14]	*Fd*-3*m*	2	Spin-liquid above T_N, antiferromagnetic below T_N	N/A	5.92	N/A	Frustration and spin-liquid behavior
$FeSc_2S_4$ [14]	*Fd*-3*m*	<0.05	Spin-orbital liquid (no long-range order)	N/A	4.9	N/A	Spin-orbital liquid state
$CoRh_2O_4$ [15]	*Fd*-3*m*	25	Collinear Néel ordered state	2.4(1)	3.87	63.5	Spin-wave corrections and quantum effects
$LiYbO_2$ [16]	$I4_1/amd$	<1	Incommensurate spiral, transitions to commensurate k=(1/3,±1/3,0)	1.26	1.5	84	Spiral ground state with frustration
$NaCeO_2$ [17]	$I4_1/amd$	3.18	A-type antiferromagnetism with Jeff=1/2 moments	0.57	2.14	26.6	Crystalline electric field effects and Jeff=1/2 state
$CuRh_2O_4$ [15]	$I4_1/amd$	24	Incommensurate helical order with reduced ordered moments	0.47(5)	1.0	47	Quantum fluctuations and frustration
$KRuO_4$ [18]	$I4_1/a$	22.4	Collinear antiferromagnet, weak frustration	0.57(7)	~1.0	57	Spin-orbit coupling and short-range spin correlations
$TbTaO_4$ [19]	*I*2/*a*	2.25	Commensurate antiferromagnetic order	7.5 (5)	9.72	0 - 77.1	Frustration and low-dimensional interactions
$CaCo_2TeO_6$	*Pmna*	17.1	Collinear antiferromagnet, spin fluctuations	3.03(1) and 2.15(1)	3.36	90 and 64	Competing interactions and quantum fluctuation

- J_1 dominates over J_2 in most cases, indicating that nearest-neighbor coupling is the primary driver of magnetic behavior.
- Large J_1/J_2 ratios (e.g., >8 for $LiYbO_2$, 25 for $KRuO_4$) suggest well-defined ground states with relatively weak frustration (e.g., $CoRh_2O_4$) favor classical Néel ordering.
- Significant next-nearest-neighbor interactions (J2) lead to competing magnetic orders (e.g., spiral or helical ground states in $LiYbO_2$ and $CuRh_2O_4$).

Table S2. Exchange interactions.

Centering Co	Distance to the same type of Co (Å)		Distance to different types of Co (Å)	
Co(1)	2.8627(6) (J_1)	3.0922(7) (J_2)	3.6131(5) (J_5)	3.7901(5) (J_6)
Co(2	2.8672(6) (J_3)	3.2139(7) (J_4)	3.6131(5) (J_5)	3.7901(5) (J_6)

Table S3. Single-crystal, synchrotron XRD data refinement.

Unit cell parameters	Single-crystal XRD	Synchrotron XRD
a (Å)	9.2519(5)	9.256351 (1)
b (Å)	8.9784(5)	8.991875 (1)
c (Å)	10.8666(6)	10.878668 (1)

Table S4. Atomic coordinates.

SXRD	x	y	z	U
Ca	0.75802(5)	1.05122(5)	0.34490(4)	0.00426(10)
Co(1)	0.56681(3)	0.90942(3)	0.60680(3)	0.00306(8)
Co(2)	0.58435(3)	0.59033(3)	0.10555(3)	0.00277(8)
Te(1)	0.43945(2)	0.750000	0.37721(2)	0.00203(7)
Te(2)	0.58421(2)	0.250000	0.10483(2)	0.00192(7)
O(1)	0.5062(2)	0.750000	0.2123(2)	0.0046(4)
O(2)	0.57286(16)	0.90733(16)	0.41961(16)	0.0037(3)
O(3)	0.30110(17)	0.59163(16)	0.34416(15)	0.0043(3)
O(4)	0.4021(2)	0.750000	0.5550(2)	0.0040(4)
O(5)	0.62146(17)	0.40957(16)	-0.00876(15)	0.0041(3)
O(6)	0.3887(2)	0.250000	0.0428(2)	0.0036(4)
O(7)	0.53159(17)	0.40627(16)	0.21923(15)	0.0039(3)
O(8)	0.7797(2)	0.250000	0.1709(2)	0.0042(4)

Synchrotron XRD	x	y	z	B
Ca	0.75802	1.05122	0.34490	1.22359
Co(1)	0.56685	0.90942	0.60924	0.97122
Co(2)	0.58483	0.59033	0.10588	0.66099
Te(1)	0.43700	0.75000	0.37867	0.65399
Te(2)	0.58208	0.25000	0.10590	0.78696
O(1)	0.50620	0.75000	0.21230	0.47481
O(2)	0.57286	0.90733	0.41961	0.33418
O(3)	0.30110	0.59163	0.34416	0.68840
O(4)	0.40210	0.75000	0.55500	0.40199
O(5)	0.62146	0.40957	-0.00876	0.41520
O(6)	0.38870	0.25000	0.04280	0.67056
O(7)	0.53159	0.40627	0.21923	0.44008
O(8)	0.77970	0.25000	0.17090	0.41797

Table S5. Phonon estimation.

Variable	Fitted value
γ	0.02671 ± 0.12987
Number of oscillators of Debye mode 1	3.7244 ± 0.79847
Debye temperature 1	393.85999 ± 39.62869
Number of oscillators of Debye mode 2	5.46047 ± 1.51089
Debye temperature 2	985.0031 ± 131.7815
Number of oscillators of Einstein mode	0.75741 ± 0.38378
Einstein temperature	112.58237 ± 15.19992
R^2	0.99978

Table S6. Magnetic vectors.

T = 1.5 K from HB-2A POWDER

Sites	M_x	M_y	M_z	Modulus (μ_B)
Co(1)	0 (Fixed)	-0.91(1)	2.07(2)	2.3(1)
Co(2)	0 (Fixed)	0.91(1)	1.16(1)	1.4(1)

T = 15 K from BL-9 CORELLI

Sites	Modulus (μ_B)
Co(1)	2.388(1)
Co(2)	2.165(1)

Vectors in Table S9

T = 15 K from HB-2A POWDER

Sites	Modulus (μ_B)
Co(1)	1.65(1)
Co(2)	2.03(1)

Vectors in Table S10

Table S7. Irreducible representations (IR) for propagation vector **q** = (0, 0, 0) and corresponding reduced χ^2 from refinement.

MSG	**IR**	**# Parameters**	**R$_{WP}$**	χ^2
Pnma (62.441)	Γ_1	6	15.5	2.871
Pn’ma (62.443)	Γ_4	6	26.8	7.789
Pnm’a (62.444)	Γ_6	6	26.1	7.356
Pnma’ (62.445)	Γ_8	6	19.1	3.968
Pn’m’a (62.446)	Γ_7	6	27.7	8.315
Pnm’a’ (62.447)	Γ_3	6	22.6	5.515
Pn’ma’ (62.448)	Γ_5	6	23.7	6.069
Pn’m’a’ (62.449)	Γ_2	6	25.5	7.021

Table S8. Neutron refinement result of the Γ_1 irreducible representations in Table S7.

Co Type	**M$_x$**	**M$_y$**	**M$_z$**	**M$_{tot}$**
Co(1)	0	-0.961	2.011	2.3(1)
Co(2)	0	0.775	1.167	1.4(1)

Γ_1	ψ_1			ψ_2			ψ_3		
	m_x	m_y	m_z	m_x	m_y	m_z	m_x	m_y	m_z
Co(1,2)_1	1	0	0	0	1	0	0	0	1
Co(1,2)_2	1	0	0	0	-1	0	0	0	-1
Co(1,2)_3	-1	0	0	0	1	0	0	0	-1
Co(1,2)_4	-1	0	0	0	-1	0	0	0	1
Co(1,2)_5	1	0	0	0	1	0	0	0	1
Co(1,2)_6	1	0	0	0	-1	0	0	0	-1
Co(1,2)_7	-1	0	0	0	1	0	0	0	-1
Co(1,2)_8	-1	0	0	0	-1	0	0	0	1

Table S9. Magnetic vectors at T = 14.5 K from BL-9 CORELLI.

```
Atom : Co(1)
----------------------------------------------------------------------------------
     x        y        z       Translation     m(a)     m(b)     m(c)     Mtot
 0.43646  0.10306  0.39676
                          (  0,   0,   0)     0.00000 -1.58129  1.78986  2.38832
                          (  0,   1,   0)     0.00000  2.01034  1.28941  2.38832
                          (  0,   2,   0)     0.00000  0.96729 -2.18367  2.38832
                          (  0,   3,   0)     0.00000 -2.30577 -0.62248  2.38832
 0.56354  0.60306  0.60324
                          (  0,   0,   0)     0.00000  2.38810 -0.03250  2.38832
                          (  0,   1,   0)     0.00000 -0.33257  2.36505  2.38832
                          (  0,   2,   0)     0.00000 -2.28653 -0.68983  2.38832
                          (  0,   3,   0)     0.00000  1.03092 -2.15436  2.38832
 0.93646  0.10306  0.10324
                          (  0,   0,   0)     0.00000  1.58129  1.78986  2.38832
                          (  0,   1,   0)     0.00000 -2.01034  1.28941  2.38832
                          (  0,   2,   0)     0.00000 -0.96729 -2.18367  2.38832
                          (  0,   3,   0)     0.00000  2.30577 -0.62248  2.38832
 0.06354  0.60306  0.89676
                          (  0,   0,   0)     0.00000 -2.38810 -0.03250  2.38832
                          (  0,   1,   0)     0.00000  0.33257  2.36505  2.38832
                          (  0,   2,   0)     0.00000  2.28653 -0.68983  2.38832
                          (  0,   3,   0)     0.00000 -1.03092 -2.15436  2.38832
 0.56354  0.89694  0.60324
                          (  0,   0,   0)     0.00000  2.01034  1.28941  2.38832
                          (  0,   1,   0)     0.00000  0.96729 -2.18367  2.38832
                          (  0,   2,   0)     0.00000 -2.30577 -0.62248  2.38832
                          (  0,   3,   0)     0.00000 -0.26306  2.37379  2.38832
 0.43646  0.39694  0.39676
                          (  0,   0,   0)     0.00000  2.38810 -0.03250  2.38832
                          (  0,   1,   0)     0.00000 -0.33257  2.36505  2.38832
                          (  0,   2,   0)     0.00000 -2.28653 -0.68983  2.38832
                          (  0,   3,   0)     0.00000  1.03092 -2.15436  2.38832
 0.06354  0.89694  0.89676
                          (  0,   0,   0)     0.00000 -2.01034  1.28941  2.38832
                          (  0,   1,   0)     0.00000 -0.96729 -2.18367  2.38832
                          (  0,   2,   0)     0.00000  2.30577 -0.62248  2.38832
                          (  0,   3,   0)     0.00000  0.26306  2.37379  2.38832
 0.93646  0.39694  0.10324
                          (  0,   0,   0)     0.00000 -2.38810 -0.03250  2.38832
                          (  0,   1,   0)    0.00000  0.33257  2.36505  2.38832
                          (  0,   2,   0)    0.00000  2.28653 -0.68983  2.38832
                          (  0,   3,   0)    0.00000 -1.03092 -2.15436  2.38832
```

```
Atom : Co(2)
--------------------------------------------------------------------------------
     x        y        z       Translation     m(a)     m(b)     m(c)     Mtot
 0.07467  0.58992  0.39579
                          (  0,   0,   0)      0.00000 -1.43317  1.62221  2.16461
                          (  0,   1,   0)      0.00000  1.82204  1.16863  2.16461
                          (  0,   2,   0)      0.00000  0.87668 -1.97913  2.16461
                          (  0,   3,   0)      0.00000 -2.08980 -0.56417  2.16461
 0.92533  0.08992  0.60421
                          (  0,   0,   0)      0.00000 -0.35963 -2.13453  2.16461
                          (  0,   1,   0)      0.00000  2.16441 -0.02945  2.16461
                          (  0,   2,   0)      0.00000 -0.30142  2.14352  2.16461
                          (  0,   3,   0)      0.00000 -2.07235 -0.62522  2.16461
 0.57467  0.58992  0.10421
                          (  0,   0,   0)      0.00000  1.43317  1.62221  2.16461
                          (  0,   1,   0)      0.00000 -1.82204  1.16863  2.16461
                          (  0,   2,   0)      0.00000 -0.87668 -1.97913  2.16461
                          (  0,   3,   0)      0.00000  2.08980 -0.56417  2.16461
 0.42533  0.08992  0.89579
                          (  0,   0,   0)      0.00000  0.35963 -2.13453  2.16461
                          (  0,   1,   0)      0.00000 -2.16441 -0.02945  2.16461
                          (  0,   2,   0)      0.00000  0.30142  2.14352  2.16461
                          (  0,   3,   0)      0.00000  2.07235 -0.62522  2.16461
 0.92533  0.41008  0.60421
                          (  0,   0,   0)      0.00000  1.82204  1.16863  2.16461
                          (  0,   1,   0)      0.00000  0.87668 -1.97913  2.16461
                          (  0,   2,   0)      0.00000 -2.08980 -0.56417  2.16461
                          (  0,   3,   0)      0.00000 -0.23842  2.15144  2.16461
 0.07467  0.91008  0.39579
                          (  0,   0,   0)      0.00000 -0.30142  2.14352  2.16461
                          (  0,   1,   0)      0.00000 -2.07235 -0.62522  2.16461
                          (  0,   2,   0)      0.00000  0.93436 -1.95257  2.16461
                          (  0,   3,   0)      0.00000  1.78698  1.22158  2.16461
 0.42533  0.41008  0.89579
                          (  0,   0,   0)      0.00000 -1.82204  1.16863  2.16461
                          (  0,   1,   0)      0.00000 -0.87668 -1.97913  2.16461
                          (  0,   2,   0)      0.00000  2.08980 -0.56417  2.16461
                          (  0,   3,   0)      0.00000  0.23842  2.15144  2.16461
 0.57467  0.91008  0.10421
                          (  0,   0,   0)      0.00000  0.30142  2.14352  2.16461
                          (  0,   1,   0)      0.00000  2.07235 -0.62522  2.16461
                          (  0,   2,   0)      0.00000 -0.93436 -1.95257  2.16461
                          (  0,   3,   0)      0.00000 -1.78698  1.22158  2.16461
```

Table S10. Magnetic vectors at T = 15 K from HB-2A POWDER

```
Atom : Co(1)
--------------------------------------------------------------------------------
      x        y        z       Translation     m(a)     m(b)     m(c)     Mtot
 0.43646  0.10306  0.39676
                          (  0,   0,   0)    0.00000 -1.01053  1.30964  1.65418
                          (  0,   1,   0)    0.00000  1.30964  1.01053  1.65418
                          (  0,   2,   0)    0.00000  1.01053 -1.30964  1.65419
                          (  0,   3,   0)    0.00000 -1.30964 -1.01053  1.65418
 0.56354  0.60306  0.60324
                          (  0,   0,   0)    0.00000  1.64061  0.21150  1.65419
                          (  0,   1,   0)    0.00000 -0.21150  1.64061  1.65419
                          (  0,   2,   0)    0.00000 -1.64061 -0.21150  1.65418
                          (  0,   3,   0)    0.00000  0.21150 -1.64061  1.65419
 0.93646  0.10306  0.10324
                          (  0,   0,   0)    0.00000  1.01053  1.30964  1.65418
                          (  0,   1,   0)    0.00000 -1.30964  1.01053  1.65418
                          (  0,   2,   0)    0.00000 -1.01053 -1.30964  1.65419
                          (  0,   3,   0)    0.00000  1.30964 -1.01053  1.65418
 0.06354  0.60306  0.89676
                          (  0,   0,   0)    0.00000 -1.64061  0.21150  1.65419
                          (  0,   1,   0)    0.00000  0.21150  1.64061  1.65419
                          (  0,   2,   0)    0.00000  1.64061 -0.21150  1.65418
                          (  0,   3,   0)    0.00000 -0.21150 -1.64061  1.65418
 0.56354  0.89694  0.60324
                          (  0,   0,   0)    0.00000  1.30964  1.01053  1.65418
                          (  0,   1,   0)    0.00000  1.01053 -1.30964  1.65418
                          (  0,   2,   0)    0.00000 -1.30964 -1.01053  1.65419
                          (  0,   3,   0)    0.00000 -1.01053  1.30964  1.65418
 0.43646  0.39694  0.39676
                          (  0,   0,   0)    0.00000  1.64061  0.21150  1.65419
                          (  0,   1,   0)    0.00000 -0.21150  1.64061  1.65419
                          (  0,   2,   0)    0.00000 -1.64061 -0.21150  1.65418
                          (  0,   3,   0)    0.00000  0.21150 -1.64061  1.65419
 0.06354  0.89694  0.89676
                          (  0,   0,   0)    0.00000 -1.30964  1.01053  1.65418
                          (  0,   1,   0)    0.00000 -1.01053 -1.30964  1.65418
                          (  0,   2,   0)    0.00000  1.30964 -1.01053  1.65419
                          (  0,   3,   0)    0.00000  1.01053  1.30964  1.65418
 0.93646  0.39694  0.10324
                          (  0,   0,   0)    0.00000 -1.64061  0.21150  1.65419
                          (  0,   1,   0)    0.00000  0.21150  1.64061  1.65419
                          (  0,   2,   0)    0.00000  1.64061 -0.21150  1.65418
                          (  0,   3,   0)    0.00000 -0.21150 -1.64061  1.65418
```

```
Atom : Co(2)
--------------------------------------------------------------------------------
     x        y        z       Translation     m(a)     m(b)     m(c)     Mtot
 0.07467  0.58992  0.39579
                             (  0,  0,  0)   0.00000 -1.23795  1.60438  2.02646
                             (  0,  1,  0)   0.00000  1.60438  1.23795  2.02646
                             (  0,  2,  0)   0.00000  1.23795 -1.60438  2.02646
                             (  0,  3,  0)   0.00000 -1.60438 -1.23795  2.02646
 0.92533  0.08992  0.60421
                             (  0,  0,  0)   0.00000  0.25911 -2.00983  2.02646
                             (  0,  1,  0)   0.00000  2.00983  0.25911  2.02646
                             (  0,  2,  0)   0.00000 -0.25911  2.00983  2.02646
                             (  0,  3,  0)   0.00000 -2.00983 -0.25911  2.02646
 0.57467  0.58992  0.10421
                             (  0,  0,  0)   0.00000  1.23795  1.60438  2.02646
                             (  0,  1,  0)   0.00000 -1.60438  1.23795  2.02646
                             (  0,  2,  0)   0.00000 -1.23795 -1.60438  2.02646
                             (  0,  3,  0)   0.00000  1.60438 -1.23795  2.02646
 0.42533  0.08992  0.89579
                             (  0,  0,  0)   0.00000 -0.25911 -2.00983  2.02646
                             (  0,  1,  0)   0.00000 -2.00983  0.25911  2.02646
                             (  0,  2,  0)   0.00000  0.25911  2.00983  2.02646
                             (  0,  3,  0)   0.00000  2.00983 -0.25911  2.02646
 0.92533  0.41008  0.60421
                             (  0,  0,  0)   0.00000  1.60438  1.23795  2.02646
                             (  0,  1,  0)   0.00000  1.23795 -1.60438  2.02646
                             (  0,  2,  0)   0.00000 -1.60438 -1.23795  2.02646
                             (  0,  3,  0)   0.00000 -1.23795  1.60438  2.02646
 0.07467  0.91008  0.39579
                             (  0,  0,  0)   0.00000 -0.25911  2.00983  2.02646
                             (  0,  1,  0)   0.00000 -2.00983 -0.25911  2.02646
                             (  0,  2,  0)   0.00000  0.25911 -2.00983  2.02646
                             (  0,  3,  0)   0.00000  2.00983  0.25911  2.02646
 0.42533  0.41008  0.89579
                             (  0,  0,  0)   0.00000 -1.60438  1.23795  2.02646
                             (  0,  1,  0)   0.00000 -1.23795 -1.60438  2.02646
                             (  0,  2,  0)   0.00000  1.60438 -1.23795  2.02646
                             (  0,  3,  0)   0.00000  1.23795  1.60438  2.02646
 0.57467  0.91008  0.10421
                             (  0,  0,  0)   0.00000  0.25911  2.00983  2.02646
                             (  0,  1,  0)   0.00000  2.00983 -0.25911  2.02646
                             (  0,  2,  0)   0.00000 -0.25911 -2.00983  2.02646
                             (  0,  3,  0)   0.00000 -2.00983  0.25911  2.02646
```

References

1. Perl J, Shin J, Schümann J, Faddegon B, Paganetti H. TOPAS: an innovative proton Monte Carlo platform for research and clinical applications. *Medical physics* 2012, **39**(11)**:** 6818-6837.

2. Coelho AA. TOPAS and TOPAS-Academic: an optimization program integrating computer algebra and crystallographic objects written in C++. *Journal of Applied Crystallography* 2018, **51**(1)**:** 210-218.

3. Rodríguez-Carvajal J. Recent advances in magnetic structure determination by neutron powder diffraction. *Physica B: Condensed Matter* 1993, **192**(1-2)**:** 55-69.

4. Blaha P, Schwarz K, Madsen GKH, Kvasnicka D, Luitz J. wien2k. *An augmented plane wave+ local orbitals program for calculating crystal properties* 2001, **60**(1).

5. Perdew JP, Burke K, Ernzerhof M. Generalized gradient approximation made simple. *Physical review letters* 1996, **77**(18)**:** 3865.

6. Giannozzi P, Baroni S, Bonini N, Calandra M, Car R, Cavazzoni C*, et al.* QUANTUM ESPRESSO: a modular and open-source software project for quantum simulations of materials. *Journal of physics: Condensed matter* 2009, **21**(39)**:** 395502.

7. Dal Corso A. Pseudopotentials periodic table: From H to Pu. *Computational Materials Science* 2014, **95:** 337-350.

8. Maintz S, Deringer VL, Tchougréeff AL, Dronskowski R. LOBSTER: A tool to extract chemical bonding from plane ‐ wave based DFT. 2016.

9. Nelson R, Ertural C, George J, Deringer VL, Hautier G, Dronskowski R. LOBSTER: Local orbital projections, atomic charges, and chemical ‐ bonding analysis from projector ‐ augmented ‐ wave ‐ based density ‐ functional theory. *Journal of Computational Chemistry* 2020, **41**(21)**:** 1931-1940.

10. Dronskowski R, Blöchl PE. Crystal orbital Hamilton populations (COHP): energy-resolved visualization of chemical bonding in solids based on density-functional calculations. *The Journal of Physical Chemistry* 1993, **97**(33)**:** 8617-8624.

11. Deringer VL, Tchougréeff AL, Dronskowski R. Crystal orbital Hamilton population (COHP) analysis as projected from plane-wave basis sets. *The journal of physical chemistry A* 2011, **115**(21)**:** 5461-5466.

12. Goodenough JB. Direct cation--cation interactions in several oxides. *Physical Review* 1960, **117**(6)**:** 1442.

13. Anderson PW. New approach to the theory of superexchange interactions. *Physical Review* 1959, **115**(1)**:** 2.

14. Fritsch V, Hemberger J, Büttgen N, Scheidt EW, Krug von Nidda HA, Loidl A*, et al.* Spin and orbital frustration in $MnSc_2S_4$ and $FeSc_2S_4$. *Physical review letters* 2004, **92**(11)**:** 116401.

15. Ge L, Flynn J, Paddison JAM, Stone MB, Calder S, Subramanian MA*, et al.* Spin order and dynamics in the diamond-lattice Heisenberg antiferromagnets $CuRh_2O_4$ and $CoRh_2O_4$. *Physical Review B* 2017, **96**(6)**:** 064413.

16. Bordelon MM, Liu C, Posthuma L, Kenney E, Graf MJ, Butch NP*, et al.* Frustrated Heisenberg J_1-J_2 model within the stretched diamond lattice of $LiYbO_2$. *Physical Review B* 2021, **103**(1)**:** 014420.

17. Bordelon MM, Bocarsly JD, Posthuma L, Banerjee A, Zhang Q, Wilson SD. Antiferromagnetism and crystalline electric field excitations in tetragonal $NaCeO_2$. *Physical Review B* 2021, **103**(2)**:** 024430.

18. Marjerrison CA, Mauws C, Sharma AZ, Wiebe CR, Derakhshan S, Boyer C*, et al.* Structure and magnetic properties of $KRuO_4$. *Inorganic Chemistry* 2016, **55**(24)**:** 12897-12903.

19. Kelly ND, Yuan L, Pearson RL, Suard E, Orench IP, Dutton SE. Magnetism on the stretched diamond lattice in lanthanide orthotantalates. *Physical Review Materials* 2022, **6**(4)**:** 044410.